The Astronomical Journal, 130:2326–2346, 2005 November

THE 2MASS WIDE-FIELD T DWARF SEARCH. IV. HUNTING OUT T DWARFS WITH METHANE IMAGING[1]

C. G. Tinney,[2] Adam J. Burgasser,[3,4] J. Davy Kirkpatrick,[5] and Michael W. McElwain[6]

Received 2005 February 19; accepted 2005 July 20

ABSTRACT

We present first results from a major program of methane filter photometry for low-mass stars and brown dwarfs. The definition of a new methane filter photometric system is described. A recipe is provided for the differential calibration of methane imaging data using existing Two Micron All Sky Survey (2MASS) photometry. We show that these filters are effective in discriminating T dwarfs from other types of stars, and we demonstrate this with Anglo-Australian Telescope observations using the IRIS2 imager. Methane imaging data and proper motions are presented for 10 T dwarfs identified as part of the 2MASS Wide-Field T Dwarf Search, seven of them initially identified as T dwarfs using methane imaging. We also present near-infrared moderate-resolution spectra for five T dwarfs newly discovered by this technique. Spectral types obtained from these spectra are compared to those derived from both our methane filter observations and spectral types derived by other observers. Finally, we suggest a range of future programs to which these filters are clearly well suited: the winnowing of T dwarf and Y dwarf candidate objects coming from the next generation of near-infrared sky surveys, the robust detection of candidate planetary-mass brown dwarfs in clusters, the detection of T dwarf companions to known L and T dwarfs via deep methane imaging, and the search for rotationally modulated time-variable surface features on cool brown dwarfs.

Key words: infrared: stars — stars: low-mass, brown dwarfs — techniques: photometric

Online material: color figures

1. BACKGROUND

T dwarfs have the coldest photospheres (at least outside our solar system) that are currently accessible to direct observation. With masses inferred to lie between $\sim 60 M_J$ and $10 M_J$, they represent a class of object linking the properties of observable low-mass stars and brown dwarfs with the properties of unobservable extrasolar planets. The defining feature of these objects is the presence of strong, broad methane absorptions in the near-infrared at 1.3–1.4, 1.6–1.8, and 2.2–2.5 μm. When first seen in the prototype T dwarf Gliese 229B (Nakajima et al. 1995), the distinctiveness of these spectroscopic features immediately suggested the need for a new spectral class. This T class was initially explored in two separate spectral typing schemes by Burgasser et al. (2002) and Geballe et al. (2002), which are in the process of being unified into a single hybrid system (Burgasser et al. 2003a).

The methane features that define T dwarfs are so broad and distinctive that the use of dedicated filters to detect them was a logical next step. Proof-of-concept observations of Gl 229B (Rosenthal et al. 1996) soon confirmed this expectation. Many more T dwarfs have been discovered in the years since, and there has been some additional exploratory work on the use of methane filters (Herbst et al. 1999; Mainzer & McLean 2003) using this larger sample of T dwarfs. Mainzer et al. (2004), in particular, have defined a four-filter narrow-bandpass photometric system in the atmospheric H window (1.45–1.8 μm) designed for the detection and characterization of young brown dwarfs in heavily reddened clusters. Golimowski et al. (2004) and Krist et al. (1998) have also presented results for methane imaging of nearby stars in a search for cool companions, based on a synthetic spectrum calibration. However, near-infrared *JHK* imaging and near-infrared spectroscopy remain the mainstay of T dwarf observational study. There has, as yet, been no large-scale characterization of observed T dwarfs using broad methane filters, nor have methane filters yet been used where they are particularly powerful: as a quick and efficient way of characterizing candidates arising from large photometric surveys as "T" or "non-T" without the need for either photometric conditions or an infrared spectrograph.

We therefore set out to more fully explore the use of methane filters in the study of T dwarfs. Three steps were critical in this process: (1) defining a photometric calibration procedure for a new photometric system (denoted CH_4s, CH_4l, and CH_4s$-$$CH_4$l) using a set of broad methane filters with IRIS2 on the 3.9 m Anglo-Australian Telescope (AAT); (2) exploring the use of Two Micron All Sky Survey (2MASS; Skrutskie et al. 1997; Cutri et al. 2003) JHK_s photometry to calibrate methane filter images differentially onto this CH_4s, CH_4l, CH_4s $-$ CH_4l photometric system; and (3) using the resulting differential methane imaging to search for T dwarfs among the lists of candidates being identified in the 2MASS Wide-Field T Dwarf Search (WFTS), a long-term program that has been conducting a search over 74% of the sky for T dwarfs in the 2MASS All-Sky database (Burgasser et al. 2003b, 2003c, 2004).

The selection criteria and selection procedures of the 2MASS WFTS are described in detail in Burgasser et al. (2003b). The most challenging aspect of this program is the extreme *rarity* of T dwarfs in a shallow magnitude-limited survey. The first-pass photometric selection criteria produce over a quarter of a million potential T dwarfs from the 1.3 billion sources in the 2MASS Point Source Catalog. But our expectation is that this sample will

[1] Based on observations obtained at the Anglo-Australian Telescope, Siding Spring, Australia.

[2] Anglo-Australian Observatory, P.O. Box 296, Epping, NSW 1710, Australia; cgt@aaoepp.aao.gov.au.

[3] Department of Astrophysics, American Museum of Natural History, Central Park West at 79th Street, New York, NY 10024; adam@amnh.org.

[4] Spitzer Fellow.

[5] Infrared Processing and Analysis Center, California Institute of Technology, Pasadena, CA 91125; davy@ipac.caltech.edu.

[6] UCLA, 8371 Mathematical Sciences, Los Angeles, CA 90095; mcelwain@astro.ucla.edu.

only contain ~20–30 *actual* T dwarfs. Visual examination of catalog images is carried out on all the first-pass candidates to eliminate ~99.5% of the faint background stars, proper-motion stars, closely separated visual binaries, and general chaff that contaminate the sample.

However, this still leaves ~1000 T dwarf candidates, which require further on-sky observations to winnow down to the much smaller number of actual T dwarfs expected. In the past, the procedure for doing this has been (Burgasser et al. 2002) near-infrared imaging to eliminate minor planets, followed by optical imaging to exclude background stars, followed by near-infrared spectroscopy to carry out final verification. The latter two steps are time-consuming and expensive in telescope time due to the faintness of these targets. Methane imaging offers the possibility of combining all three of these steps into one observation. A pair of 2–3 minute methane exposures on a 4 m class telescope can (1) reveal whether there is still an infrared object present at the 2MASS position (i.e., eliminate uncataloged minor planets), (2) reveal the color of the object in the methane filters (which can determine its T or non-T nature and estimate T spectral type), and (3) automatically provide proper-motion data. Follow-up infrared spectroscopy, therefore, need only be carried out on a much smaller sample of high-confidence T dwarf candidates, rather than the hundreds otherwise required. The greatly reduced data processing overhead of a pair of methane images, compared to that of infrared images, optical images, and infrared spectroscopy, is also a significant advantage.

This is Paper IV in the series arising from the WFTS. Paper I (Burgasser et al. 2003b) describes the selection process for our T dwarf candidates in detail. Papers II and III (Burgasser et al. 2003c, 2004) present initial T dwarf discoveries arising from the search. In this paper we describe the definition of a new CH_4s, CH_4l, $CH_4s - CH_4l$ photometric system using methane filters, provide sequences relating infrared *JHK* colors to these methane colors, and describe a procedure for using 2MASS data to differentially calibrate observations onto that system. We present IRIS2 $CH_4s - CH_4l$ data and proper motions for new T dwarfs identified by this program—five new T dwarfs and a number of T dwarfs previously published by us (Burgasser et al. 2003c, 2004), many of which were independently detected by our methane imaging in 2002–2003. In § 3.1 we present spectra for a number of these new T dwarfs, obtained with the IRIS2 instrument, and demonstrate that these spectra confirm our methane filter detections. Finally, § 4 discusses the extension of these techniques into other areas of T dwarf research.

2. METHANE IMAGING

2.1. *Imaging with IRIS2*

IRIS2 is an all-refracting, nine-element, focal-reducing collimator camera, which is installed at the AAT's f/8 Cassegrain focus. It provides a final f-ratio at its HAWAII1 HgCdTe detector of f/2.2, or a plate scale of 0.″4486 pixel^{-1}. This results in a field of view 7.′7 on a side. The optical train is capable of delivering 1 pixel FWHM images over the whole field of view. However, as with all focal reduction systems of this type, it introduces astrometric distortion into the detected images. IRIS2's astrometric distortion is such that the plate scale in the corners of the detector is ~1% smaller than that at the field center. It is quite precisely represented as a radial distortion, which can be parameterized by a quartic polynomial of the form

$$r = r'\left(1 - 2.4988 \times 10^{-6} r' - 4.4466 \times 10^{-11} r'^{3}\right), \quad (1)$$

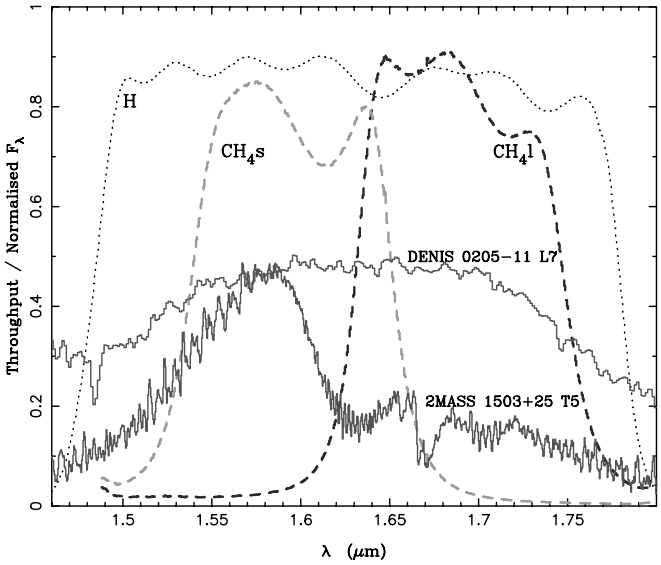

FIG. 1.—IRIS2 methane filters. The thick dashed lines show the measured bandpasses of the IRIS2 CH_4s and CH_4l filters. The cut-on, central, and cutoff wavelengths for the CH_4s and CH_4l filters are 1.520, 1.570, and 1.620 μm and 1.640, 1.690, and 1.740 μm, respectively. For comparison, the MKO *H* filter bandpass (also installed in IRIS2) is plotted as a dotted line. Spectra of the T5 dwarf 2MASS J15031961+2525196 (*lower solid line*; SpeX data from Burgasser et al. 2004) and the L7 dwarf DENIS-P J0205.4−1159 (*upper solid line*; CGS4 data from Leggett et al. 2001) are also shown. The two spectra have been normalized at 1.57 μm. [*See the electronic edition of the Journal for a color version of this figure.*]

where r' is the radius in observed pixels from a central pixel $(x_0, y_0) = (516.86, 515.02)$, and r is the radius in pixels from (x_0, y_0) in an ideal undistorted coordinate system with plate scale 0.″4486 pixel^{-1}.[7]

IRIS2 contains a filter set acquired as part of one of the Mauna Kea Observatories infrared filter consortia. A set of *J*, *H*, *K*, and K_s filters was acquired from OCLI of Santa Rosa, California, in 1998, and sets of narrowband and intermediate-band filters were acquired from NDC Infrared Engineering, Essex, UK, between 2000 and 2002. The *J*, *H*, *K*, and K_s filters were manufactured to the "Mauna Kea Observatories Near-Infrared Filter Set" specifications of Tokunaga et al. (2002). The narrowband and intermediate-band sets are as specified by A. Tokunaga.[8] In particular, the latter set includes a pair of methane filters, which we denote CH_4s and CH_4l, which are available in many other infrared instruments at telescopes around the world. Figure 1 shows the bandpasses for these filters, superposed on T and L dwarf spectra. The CH_4l filter samples the broad 1.6–1.8 μm methane absorption bands seen in T dwarfs, while the CH_4s filter samples the pseudocontinuum outside the methane band—although, as for all cool dwarf photospheres, this pseudocontinuum is itself the result of significant molecular absorption, in this case largely H_2O.

2.2. *IRIS2 Observations*

Imaging observations in methane filters were acquired (in combination with a variety of other observing programs) on 29 nights in the period 2002 March 31 to 2004 March 9 with IRIS2. Observing conditions on these nights were highly variable, from good seeing in photometric conditions to poor seeing in partial cloud. (In many cases methane observations were carried out as a "poor conditions" backup to other observing programs.)

[7] See the IRIS2 Web site at http://www.aao.gov.au/iris2/iris2.html for details.
[8] See http://www.ifa.hawaii.edu/~tokunaga/NB_special_ordersorting.html.

TABLE 1
CH_4s AND CH_4l PHOTOMETRIC PARAMETERS

	Air-Mass Correction (A)[a]		Zero Point (ZP)	
Night	CH_4s	CH_4l	CH_4s	CH_4l
2002 Oct 21	0.03 ± 0.03	0.03 ± 0.03	10.46 ± 0.03	10.46 ± 0.02
2003 Jan 25.....	0.03 ± 0.03	0.03 ± 0.03	10.76 ± 0.02	10.76 ± 0.02
2004 Mar 1	0.42 ± 0.01	0.45 ± 0.01	10.35 ± 0.06	10.35 ± 0.06

[a] Calibrated magnitude $= -2.5 \log_{10}(\text{counts}/t_{\text{exp}}) - A \times \text{air mass} + 31 - \text{ZP}$.

Objects targeted for observation over the course of this program included known T dwarfs, known L dwarfs, a large number of candidate T dwarfs derived from the 2MASS WFTS, and (in photometric conditions) United Kingdom Infrared Telescope (UKIRT) Faint Standard (FS) stars (Hawarden et al. 2001).

Observations with these filters are carried out by obtaining a series of dithered individual exposures in each filter. All these observations are performed under the control of an IRIS2 observing sequence, providing dithers in either fixed or pseudo-random patterns. As data are taken, they are processed online using an implementation of the ORAC-DR data reduction pipeline.[9] ORAC-DR is a generic data reduction pipeline originally created at the Joint Astronomy Centre, Hawaii, for use with various UKIRT and James Clerk Maxwell Telescope instruments. It collects sets of observations of a target in a single filter into a *group*. It generates a first-pass flat field for the group by suitably normalizing and creating a median image. It uses these first-pass flattened data to detect objects, mask them out, and flag bad pixels. It then creates a final flat field by taking the median of these normalized and masked data and applying it to the raw data to create a *flattened group*. The flattened group images are resampled to remove astrometric distortion, objects are redetected, and offsets between images are estimated using these detections. The images are then resampled again onto a uniform coordinate system to create a single *final* image. All of this processing is carried out on a dedicated data reduction 3.3 Ghz Linux PC, resulting in fully processed images within 30 s of completion of an observing sequence—usually before the telescope has even been moved to the next observing target.

2.3. *A Methane Photometric System*

To calibrate the methane colors of T dwarfs, extensive observations of both UKIRT FS stars and known M, L, and T dwarfs were obtained on at least three photometric nights over the course of our observing program: 2002 October 21, 2003 January 25, and 2004 March 1. There are no preexisting photometric standards for use with such filters, so we elected to define our own photometric system based on the Mauna Kea Observatories (MKO) *H*-band photometry of UKIRT FS stars.[10] Additional *JHK* photometry on the same MKO system for a number of M, L, and T dwarfs was obtained from Leggett et al. (2002) and Knapp et al. (2004). Where MKO *JHK* photometry for M, L, and T dwarfs observed in the methane filters was not available, we converted 2MASS photometry (Cutri et al. 2003) to the MKO system using published spectral types and the conversion functions of Stephens & Leggett (2004).

Aperture photometry was measured for all the targets observed on these nights. For bright targets, large photometric apertures (10″–15″ in radius) were chosen, resulting in <0.005 mag in flux being missed outside the aperture. For fainter targets, photometry was performed in smaller (2″–4″ radius) apertures, and bright objects in the same image were used to determine aperture corrections to the same large apertures as used for brighter objects. Uncertainties due to the standard error in the mean of these aperture corrections (estimated on an image-by-image basis) and the <0.005 mag flux potentially missed outside the outer aperture were carried through all subsequent calculations.

We adopted UKIRT FS stars of spectral types A, F, and G as fundamental standards. This spectral type range was chosen because (as we show below) it shows essentially zero CH_4s-CH_4l color variation. We assign to these UKIRT FS stars magnitudes in the CH_4s and CH_4l filters identical to their MKO *H* magnitudes and from this determine photometric calibrations (both air-mass corrections and zero points) on each night. These are reported in Table 1. In all but one case, the CH_4s and CH_4l air-mass corrections and zero points were consistent with being the same (on a given night), so average values were adopted and are reported in the table. The exception was 2004 March 1, when the air-mass corrections were not consistent with a single value, and so different values were used. Both air-mass corrections on this night were also significantly larger than those obtained on the other two nights, and the photometric zero point has significantly larger uncertainties. This night was warm, humid, and somewhat hazy, which is thought to be the reason for the larger extinction and poorer photometric accuracy. There is also significant variation from night to night in the photometric zero point. These variations most likely reflect the fact that these filters sample the edges of the atmospheric water vapor absorption bands that define the *H* window (at least at the Siding Spring site). Night-to-night variations in the amount of water vapor absorption will result in differing zero points. However, since the critical parameter these filters measure is the *difference* between CH_4s and CH_4l, as long as observations in the two filters are closely spaced in time and air mass, these variations are essentially irrelevant.

2.4. *Methane Photometry*

2.4.1. $CH_4s - CH_4l$ *and Spectral Type*

These observations therefore provide photometry in CH_4s, CH_4l, and, most importantly, $CH_4s - CH_4l$ color. Figure 2

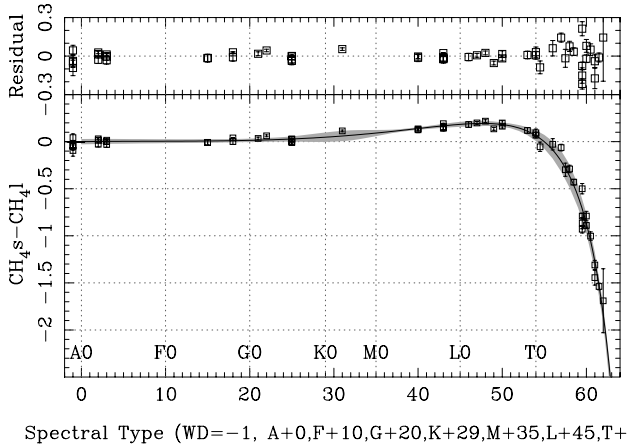

FIG. 2.—IRIS2 methane color ($CH_4s - CH_4l$) as a function of A–T spectral type. The uncertainties plotted are the combination of photon-counting uncertainties, aperture correction uncertainties, and photometric calibration uncertainties. Typical uncertainties on spectral types (not plotted) are ±0.5. See the text for references to the spectral type sources and for the form of the plotted parameterization. The rms scatter about the parameterization (*gray shading*) is 0.07 mag for the whole range, 0.04 mag for L0–T2 dwarfs, and 0.11 mag for T dwarfs.

[9] See http://www.oracdr.org.
[10] See http://www.jach.hawaii.edu/UKIRT/astronomy/calib/phot_cal.

TABLE 2

$CH_4s - CH_4l$ AND *JHK* PHOTOMETRY FOR A–T DWARFS

Short Name	Full Name	Spectral Type	n[a]	$J - H_{MKO}$[b]	$H - K_{MKO}$[b]	$J - K_{MKO}$[b]	$CH_4s - CH_4l$[c]	$(CH_4s - CH_4l)_{Diff}$[d]	References (Spectral Type)[e]	References (*JHK*)[f]
					UKIRT FS					
FS 10	GD 50	DA	−1	−0.05	−0.14	−0.19	−0.09 ± 0.06 (1)	−0.11 ± 0.04 (1)	1	1
FS 20	EG 76	DA	−1	−0.01	−0.05	−0.07	−0.04 ± 0.05 (1)	−0.06 ± 0.02 (1)	1	1
FS 34	EG 141	DA	−1	−0.04	−0.09	−0.12	0.00 ± 0.03 (2)	−0.02 ± 0.01 (2)	1	1
FS 7	SA 94−242	A2	2	0.12	0.01	0.13	0.01 ± 0.02 (3)	+0.06 ± 0.02 (3)	2	1
FS 11	SA 96−83	A3	3	0.07	0.03	0.09	−0.01 ± 0.02 (3)	+0.04 ± 0.01 (3)	2	1
FS 2	SA 92−342	F5	15	0.19	0.03	0.22	−0.01 ± 0.03 (1)	−0.03 ± 0.01 (1)	2	1
FS 4	SA 93−317	F5	15	0.23	0.03	0.27	−0.01 ± 0.03 (1)	+0.01 ± 0.01 (1)	2	1
FS 18	SA 100−280	F8	18	0.24	0.05	0.29	0.02 ± 0.02 (2)	+0.07 ± 0.01 (2)	2	1
FS 137	...	G1	21	0.25	0.05	0.30	0.03 ± 0.02 (1)	+0.02 ± 0.01 (2)	2	1
FS 16	...	G1	21	0.29	0.06	0.34	0.06 ± 0.01 (1)	+0.03 ± 0.01 (1)	2	1
FS 13	SA 97−249	G4	24	0.31	0.05	0.36	0.00 ± 0.01 (3)	+0.04 ± 0.01 (3)	2	1
FS 135	...	G5	25	0.30	0.06	0.35	0.03 ± 0.01 (1)	+0.06 ± 0.01 (1)	2	1
FS 136	...	K2	31	0.52	0.12	0.64	0.11 ± 0.01 (1)	+0.09 ± 0.02 (1)	2	1
FS 124	LHS 254	M5	40	0.40	0.34	0.74	0.13 ± 0.03 (1)	+0.18 ± 0.01 (1)	3	1
FS 128	...	M5	40	0.55	0.38	0.93	0.14 ± 0.02 (1)	+0.16 ± 0.01 (1)	3	1
FS 129	LHS 2397a	M8(+L7)	43	0.63	0.54	1.17	0.16 ± 0.01 (4)	+0.21 ± 0.01 (4)	3	1
					L Dwarfs					
2M 1045−0149	2MASS J10452400−0149576	L1	46	0.65	0.63	1.27	0.18 ± 0.03 (1)	+0.17 ± 0.01 (1)	4	2
Kelu-1	2MASS J13054019−2541059	L2	47	0.78	0.67	1.45	0.20 ± 0.02 (1)	+0.23 ± 0.02 (1)	5	3
DEN 1058−1548	DENIS-P J1058.7−1548	L3	48	0.84	0.74	1.57	0.22 ± 0.02 (1)	+0.23 ± 0.02 (1)	5	3
DEN 1539−0520	DENIS-P J153941.96−052042.4	L4	49	0.69	0.57	1.26	0.14 ± 0.02 (1)	+0.08 ± 0.16 (1)	6	2
DEN 1228−1547	DENIS-P J1228.2−1547AB	L5	50	0.88	0.69	1.57	0.20 ± 0.03 (1)	+0.23 ± 0.02 (1)	5	3
2M 1507−1627	2MASS J15074769−1627386	L5	50	0.75	0.67	1.42	0.16 ± 0.02 (1)	+0.20 ± 0.01 (1)	5	2
DEN 0255−4700[g]	DENIS-P J0255.0−4700	L8	53	0.83	0.74	1.57	0.12 ± 0.03 (1)	+0.18 ± 0.01 (1)	5	4

TABLE 2—*Continued*

Short Name	Full Name	Spectral Type	n[a]	$J - H_{MKO}$[b]	$H - K_{MKO}$[b]	$J - K_{MKO}$[b]	$CH_4s - CH_4l$[c]	$(CH_4s - CH_4l)_{Diff}$[d]	References (Spectral Type)[e]	References (JHK)[f]
				T Dwarfs						
SD 0423−0414	SDSSp J042348.57−041403.5	T0	54	0.79	0.55	1.34	0.08 ± 0.03 (2)	+0.15 ± 0.02 (4)	7	2
SD 1207+0244	SDSSp J120747.17+024424.8	T0.5	54.5	0.75	0.47	1.22	−0.05 ± 0.05 (1)	+0.05 ± 0.03 (1)	7	2
SD 1254−0122	SDSSp J125453.90−012247.4	T2	56	0.53	0.29	0.82	−0.03 ± 0.06 (1)	+0.04 ± 0.02 (1)	7	2
SD 1021−0304	SDSSp J102109.69−030420.1	T3.5	57.5	0.47	0.15	0.62	−0.30 ± 0.07 (1)	−0.11 ± 0.04 (4)	7	2
SD 0207+0000	SDSSp J020742.83+000056.2	T4	58	0.01	−0.03	0.04	−0.29 ± 0.04 (1)	−0.37 ± 0.10 (1)	7	2
2M 0559−1404	2MASS J05591914−1404488	T4.5	58.5	−0.16	−0.07	−0.09	−0.43 ± 0.03 (1)	−0.40 ± 0.02 (3)	7	2
2M 0516−0445	2MASS J05160945−0445499	T5.5	59.5	−0.06	0.16	0.10	−0.79 ± 0.03 (1)	−0.70 ± 0.02 (3)	8	4
SD 1110+011	SDSSp J111010.01+011613.1	T5.5	59.5	−0.10	0.17	0.07	−0.69 ± 0.20 (2)	−0.66 ± 0.12 (2)	7	2
2M 2356−1553	2MASS J23565477−1553111	T5.5	59.5	−0.22	−0.03	−0.25	−0.93 ± 0.04 (1)	−0.71 ± 0.05 (4)	7	2
2M 0243−2453	2MASS J02431371−2453298	T6	60	−0.26	0.05	−0.21	−0.79 ± 0.05 (1)	−0.77 ± 0.02 (3)	7	2
2M 2228−4310	2MASS J22282889−4310262	T6	60	−0.05	−0.03	−0.08	−0.89 ± 0.03 (1)	−0.82 ± 0.02 (1)	7	2
SD 1346−0031	SDSSp J134646.45−003150.4	T6.5	60.5	−0.35	0.11	−0.24	−1.00 ± 0.05 (1)	−0.87 ± 0.08 (1)	7	2
2M 1217−0311	2MASS J12171110−0311131	T7	61	−0.42	0.06	−0.36	−1.44 ± 0.08 (1)	−1.42 ± 0.08 (1)	7	2
Gl 570d	2MASS J14571496−2121477	T7.5	61.5	−0.46	−0.24	−0.70	−1.54 ± 0.04 (1)	−1.38 ± 0.05 (4)	7	2
2M0415−0935	2MASS J04151954−0935066	T8	62	−0.51	−0.38	−0.13	−1.69 ± 0.34 (1)	−1.66 ± 0.05 (3)	7	2

[a] The variable n is the spectral subtype plus a constant for A–T dwarfs: 0 for an A dwarf, 10 for F, 20 for G, 29 for K, 35 for M, 45 for L, and 54 for T. It is set to the placeholder value of −1 for white dwarfs.

[b] $J - H$, $H - K$, and $J - K$ on the MKO photometric system. Typical uncertainties are <0.01 mag for UKIRT FS standards and <0.05 mag for the remaining objects.

[c] The number of observations averaged to provide the quoted result is indicated in parentheses.

[d] See § 2.5 for definition of $(CH_4s - CH_4l)_{Diff}$. The number of observations averaged to provide the quoted result is indicated in parentheses.

[e] (1) McCook & Sion 1999; (2) Hawarden et al. 2001; (3) Leggett et al. 2002; (4) Gizis 2002; (5) Kirkpatrick et al. 2000; (6) D. Kirkpatrick 2005 (private communication) and determined using optical spectroscopy to estimate spectral types on the Kirkpatrick et al. 2000 system; (7) Burgasser et al. 2005; (8) Burgasser et al. 2003c.

[f] (1) UKIRT MKO photometric standards (see § 2.3); (2) Knapp et al. 2004; (3) Leggett et al. 2002; (4) converted 2MASS data into the MKO system using the conversion relations of Stephens & Leggett 2004.

[g] The conversions from 2MASS to MKO photometry of Stephens & Leggett (2004) are essentially independent of the spectral-typing system for early to mid-L and T dwarfs but are less so for late-type L dwarfs. In the case of DENIS-P J0255.0−4700, this could lead to an additional uncertainty in its MKO colors of <0.03 mag over and above the 0.05 mag relevant for the other L and T dwarfs so converted.

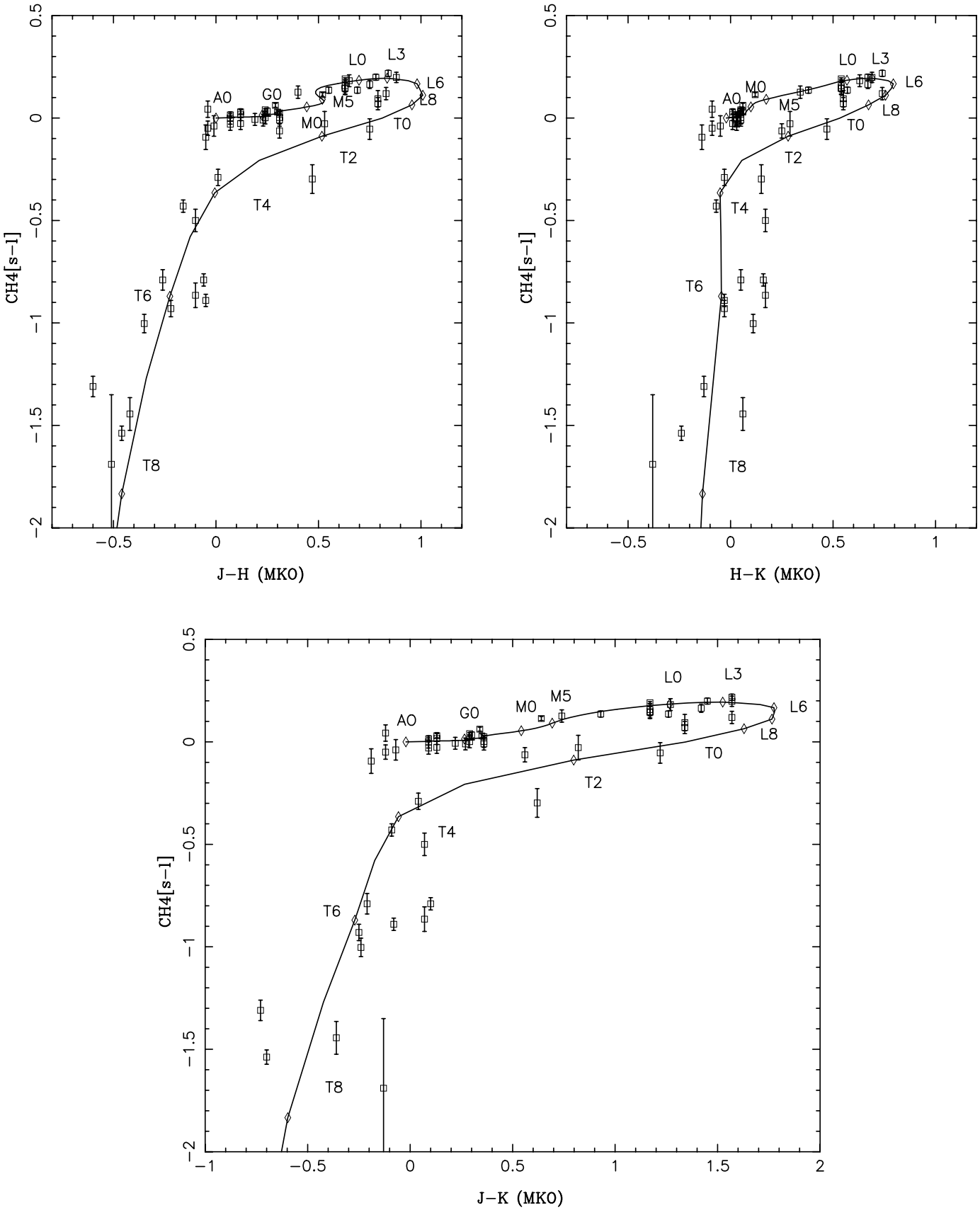

FIG. 3.—IRIS2 methane color ($CH_4s - CH_4l$) as a function of $J - H$, $H - K$, and $J - K$ (MKO) color. The $CH_4s - CH_4l$ uncertainties plotted are the combination of photon-counting uncertainties, aperture correction uncertainties, and photometric calibration uncertainties. *JHK* photometry and uncertainties are from the UKIRT World Wide Web pages, MKO photometry is from Leggett et al. (2002), and 2MASS photometry is converted to the MKO system using the conversion relations of Stephens & Leggett (2004). The overplotted tracks and spectral types (*solid lines and open diamonds*) are produced from the $CH_4s - CH_4l$ vs. spectral type relation of Fig. 2 and the *JHK* color vs. spectral type relations of Fig. 4 and Table 3. Note the four white dwarf observations that, when plotted in this plane, lie just to the left of the A0 end of the plotted sequence.

shows $CH_4s - CH_4l$ color as a function of spectral type. Spectral type is parameterized numerically as n, such that for A- to T-type stars n is the spectral subtype plus a constant: 0 for an A dwarf, 10 for F, 20 for G, 29 for K, 35 for M, 45 for L, and 54 for T. While it was not our intention in this work to study the detailed methane spectroscopy of white dwarfs, nonetheless three UKIRT FS white dwarfs were observed during the course of this program, which we have put at the placeholder position of $n = -1$. The objects plotted (and tabulated in Table 2) are as follows: UKIRT FS stars with spectral types A–K for stars from Hawarden et al. (2001) and for white dwarfs from McCook & Sion (1999); M dwarfs with Leggett et al. (2002) spectral types; L dwarfs with Kirkpatrick et al. (2000) types, except for 2MASS 1045−0149 (Gizis 2002) and DENIS 1539−0520, which is based on a Keck optical spectrum analyzed so as to place it on the Kirkpatrick et al. (2000) system (D. Kirkpatrick 2005, private communication); and T dwarfs with spectral types on a variant of the hybrid T-typing scheme that was preliminarily proposed by Burgasser et al. (2003a) but modified to use slightly different indices and spectroscopic reference standards, as described in § 3.2. Table 2 also provides the average $CH_4s - CH_4l$ colors for all the objects in Figure 2, along with the spectral types and *JHK* colors adopted, so that others using such filters can calibrate their data onto a uniform system.

As suggested above, the variation in $CH_4s - CH_4l$ color across the A, F, and G spectral types is negligibly small, which is why these stars were chosen to define the photometric system. K, M, and L dwarfs have slightly positive $CH_4s - CH_4l$ colors (i.e., they are red in these filters), while T dwarfs show a marked trend to become bluer with increasing T spectral type. Figure 2 also shows a parameterization for this relationship, as follows:

$$CH_4s - CH_4l = n\left(0.0087 + 6.176\times10^{-6}n^2 + 1.202\times10^{-9}n^4 - \frac{0.519}{68.5 - n}\right). \quad (2)$$

While this function is numerically valid to $n < 68.5$, it is only constrained by data in the range $0 < n < 62$ (i.e., the white dwarfs do not constrain the fit). The rms scatter about this fit is 0.07 mag over the whole spectral-type range. More critically, the rms scatter is 0.11 mag for T dwarfs and 0.04 mag for L0–T2 dwarfs.

2.4.2. $CH_4s - CH_4l$ *and JHK Colors*

While this $CH_4s - CH_4l$ relationship is useful for assigning T spectral types, it is not the only tool for examining the potential T dwarfs in large photometric surveys like 2MASS or the forthcoming UKIRT Infrared Deep Sky Survey (UKIDSS;[11] Hambly et al. 2003). These surveys will also produce *JHK* photometry, providing additional data on whether a given object is likely to be a T dwarf.

Figure 3 shows plots of $CH_4s - CH_4l$ color as a function of $J - H$, $H - K$, and $J - K$ color (on the MKO photometric system) for the objects (except the white dwarfs) presented in Figure 2. The *JHK* photometry for these objects comes (in order of preference) from the UKIRT MKO photometric standards database,[12] from Leggett et al. (2002), from Knapp et al. (2004), or by converting 2MASS data into the MKO system using the conversion relations of Stephens & Leggett (2004). Clearly, the dwarf

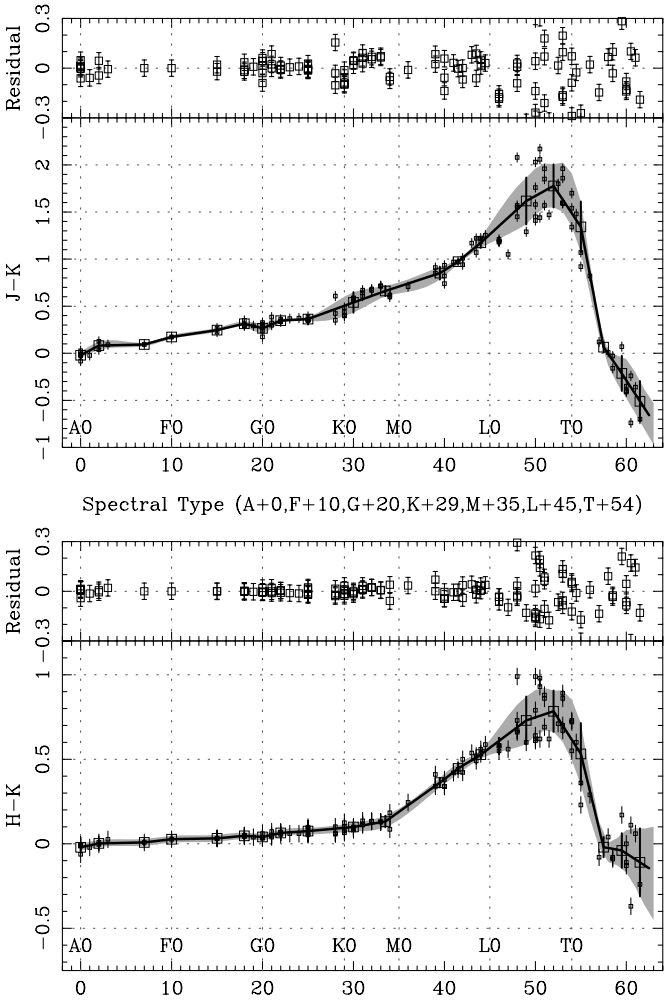

FIG. 4.—$J - K$ and $H - K$ (MKO) as a function of A–T spectral type. *JHK* photometry and uncertainties are from the UKIRT World Wide Web pages, and the MKO photometry is from Leggett et al. (2002) for M, L, and T dwarfs (*small squares*). These data have been binned by spectral type (*large squares*), which have themselves been fitted with a cubic spline interpolating function (*solid line*). The shaded region shows the 1 σ rms scatter about the binning. These tracks are summarized in Table 3.

sequence has a complex behavior in these diagrams, with the added complication of significant scatter among the T dwarfs.

To try and clarify this behavior, we have combined the $CH_4s - CH_4l$ versus spectral type relations derived above with the *JHK* versus spectral type sequences for dwarf stars. The latter have been derived using the spectral types of Hawarden et al. (2001) for UKIRT MKO photometric standards supplemented by published M, L, and T types (see §§ 2.4.1 and 3.2 for details and references) for a number of cool dwarfs with existing MKO *JHK* photometry (Leggett et al. 2002; Knapp et al. 2004). The resulting sequences are shown in Figure 4. Tests with polynomials of both low and high order show that these curves are not readily amenable to simple parameterization, so we have parameterized the $J - K$ and $H - K$ sequences by binning the available data by spectral type (*large squares*) and interpolating a cubic spline through these data points (*solid line*).

These near-infrared sequences, combined with the $CH_4s - CH_4l$ versus spectral type sequences derived above, produce "tracks" in the $CH_4s - CH_4l$ versus color planes, which are shown in Figure 3. These tracks tell us (among other things) that to discriminate between early T dwarfs and the M–L dwarfs, $CH_4s - CH_4l$ photometry must be sufficiently precise to reveal

[11] See http://www.ukidss.org.
[12] See http://www.jach.hawaii.edu/UKIRT/astronomy/calib/phot_cal.

TABLE 3
SPECTRAL TYPE, METHANE, AND *JHK* COLOR SEQUENCES

		MKO			2MASS		
SPECTRAL TYPE	$CH_4s - CH_4l$[a]	$J - H$[b]	$H - K$[b]	$J - K$[b]	$J - H$[c]	$H - K$[c]	$J - K$[c]
A0	+0.000	+0.000	−0.021	−0.021	−0.038	−0.002	−0.023
A5	+0.004	+0.087	+0.006	+0.093	+0.063	+0.021	+0.095
F0	+0.005	+0.146	+0.027	+0.173	+0.131	+0.039	+0.178
F5	+0.007	+0.214	+0.032	+0.246	+0.209	+0.044	+0.254
G0	+0.014	+0.225	+0.040	+0.265	+0.222	+0.051	+0.274
G5	+0.028	+0.288	+0.075	+0.363	+0.295	+0.081	+0.375
K0	+0.047	+0.407	+0.092	+0.499	+0.432	+0.096	+0.516
K3	+0.067	+0.504	+0.110	+0.614	+0.545	+0.112	+0.636
M0	+0.091	+0.519	+0.174	+0.693	+0.562	+0.167	+0.718
M2	+0.110	+0.495	+0.252	+0.747	+0.534	+0.235	+0.774
M4	+0.129	+0.486	+0.340	+0.826	+0.524	+0.311	+0.856
M6	+0.149	+0.512	+0.426	+0.938	+0.554	+0.386	+0.972
M8	+0.168	+0.595	+0.495	+1.090	+0.650	+0.446	+1.129
L0	+0.184	+0.698	+0.568	+1.266	+0.853	+0.538	+1.391
L2	+0.193	+0.792	+0.651	+1.443	+0.958	+0.579	+1.537
L4	+0.190	+0.878	+0.723	+1.601	+1.056	+0.633	+1.689
L6	+0.167	+0.981	+0.794	+1.775	+1.173	+0.706	+1.879
L8	+0.111	+1.009	+0.756	+1.765	+1.218	+0.685	+1.903
T0	+0.064	+0.956	+0.673	+1.629	+1.176	+0.615	+1.791
T1	−0.001	+0.810	+0.532	+1.342	+1.041	+0.490	+1.531
T2	−0.089	+0.517	+0.281	+0.798	+0.761	+0.257	+1.018
T3	−0.207	+0.211	+0.055	+0.266	+0.470	+0.050	+0.520
T4	−0.365	−0.006	−0.051	−0.057	+0.269	−0.036	+0.233
T5	−0.579	−0.126	−0.047	−0.173	+0.167	−0.012	+0.156
T6	−0.870	−0.225	−0.045	−0.270	+0.088	+0.011	+0.099
T7	−1.270	−0.340	−0.083	−0.423	−0.004	−0.007	−0.012
T8	−1.834	−0.460	−0.137	−0.597	−0.100	−0.042	−0.142

[a] Sequence represented by eq. (2).
[b] Spline sequences as shown in Fig. 4.
[c] MKO sequences converted to 2MASS system as described in the text.

the 0.2 mag gap between these two classes of object. The sequences are tabulated in Table 3.

One notable feature of these tracks is the inflection at $J - H \approx 0.5$ in the $J - H$ versus $CH_4s - CH_4l$ plane, which is simply the mapping into $J - H$ versus $CH_4s - CH_4l$ of the well-known inflection in the $J - H$ versus $H - K$ diagram, which is produced as giants bifurcate from dwarfs at mid-M spectral types (see, e.g., Fig. A3 of Bessell & Brett 1988).

2.5. *Differential Methane Photometry*

While photometry is essential to underpin our determination of the relationship between near-infrared color, spectral type, and $CH_4s - CH_4l$ color, the observational overheads in obtaining such data are large, leading us to ask, Can we make do with differential photometry? Since both our bands can be observed nearly simultaneously at identical air masses in similar seeing and transparency conditions, systematic uncertainties in aperture corrections due to seeing variations, extinction corrections due to air-mass variations, and (to some extent) zero-point corrections due to transparency variations can all be canceled out. The availability of the 2MASS data provides an additional incentive to the differential approach, since *H*-band calibration photometry is available over almost 100% of the sky.

Our $CH_4s - CH_4l$ photometric system is defined based on MKO *H* photometry for standard stars of spectral type A, F, and G or, equivalently, in color space $-0.021 < (J - K)_{MKO} < 0.456$, $-0.021 < (H - K)_{MKO} < 0.086$, or $0.00 < (J - H)_{MKO} < 0.370$. To use 2MASS photometry to calibrate the same data, we can transform these color ranges into the appropriate 2MASS ranges using the conversions provided by the 2MASS Explanatory Supplement[13] for A–M dwarfs, supplemented by the conversions of Stephens & Leggett (2004) for L–T dwarfs. Figure 5 shows the $CH_4s - CH_4l$ versus $(J - H)_{MKO}$ relation derived above, along with the comparable $CH_4s - CH_4l$ versus $(J - H)_{2MASS}$ relation obtained by transforming MKO colors to 2MASS colors. ($J - H$ has been chosen for this plot because it is the color most commonly available for objects in the 2MASS catalog; similar relations have been derived for the other *JHK* colors.) In principle, therefore, one could select background stars in a pair of CH_4s and CH_4l frames with 2MASS colors corresponding to A–G spectral types $-0.023 < (J - K)_{2MASS} < 0.472$, $-0.002 < (H - K)_{2MASS} < 0.091$, or $-0.038 < (J - H)_{2MASS} < 0.390$. Unfortunately, even with a field of view as large as that of IRIS2 (7.′7 on a side), this often restricts the number of objects available for calculating a zero point to less than 2 per field.

However, Figure 5 indicates that a much larger range of colors could be used to calculate a zero point if one were able to parameterize the variation in $CH_4s - CH_4l$ as a function of 2MASS color. The solid lines in Figure 5 represent a parameterization for $(J - H)_{2MASS}$ that has been adopted to do this. We avoid the region $0.5 < (J - H)_{2MASS} < 0.6$, where the sequence is degenerate, and fit two separate quadratics to the regions $-0.05 < (J - H)_{2MASS} < 0.5$,

$$CH_4s - CH_4l = -0.0015 - 0.0.00864(J - H) + 0.2569263(J - H)^2 \quad (3)$$

[13] See http://www.ipac.caltech.edu/2mass/releases/allsky/doc/sec6_4b.html.

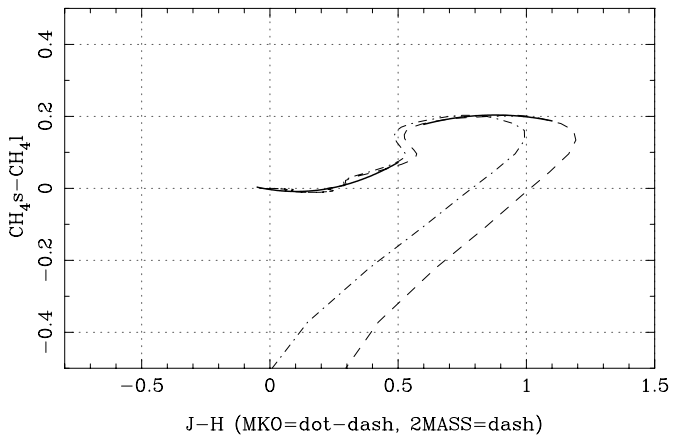

FIG. 5.—$CH_4s - CH_4l$ dwarf sequence as a function of $J - H$ in the MKO and 2MASS systems. The MKO curve (*dot-dashed line*) comes from the parameterizations in Fig. 3, and the 2MASS curve (*dashed line*) is the MKO curve transformed using the conversions in the 2MASS Explanatory Supplement and Stephens & Leggett (2004). The solid lines are polynomial fits to ranges $(J - H)_{MKO} = -0.05$ to 0.5 and 0.6–1.1, which are nondegenerate and useful for determining the $CH_4s - CH_4l$ zero point of observations with 2MASS photometry.

and $0.6 < (J - H)_{2MASS} < 1.1$,

$$CH_4s - CH_4l = -0.0378 + 0.47851(J - H) - 0.249901(J - H)^2. \quad (4)$$

Of course, these relations are also degenerate with the T dwarf branch of the sequence. We therefore adopt a two-stage calibration approach: by rejecting from the second pass any objects within 10″ of any known or suspected T dwarfs in the field and any objects with $CH_4s - CH_4l < -0.2$, we eliminate any T dwarfs that might contaminate this calibration.

The following procedure, therefore, enables the use of the ensemble of background stars in a field of view to derive a robust differential $CH_4s - CH_4l$ in even nonphotometric conditions:

1. Select and photometer stars in CH_4s and CH_4l images. We carried out this step using the Starlink implementation of SExtractor[14] (Bertin & Arnouts 1996). It is important to note that the detailed parameters used in this process are not critical, since the only aim is to obtain robust *relative* photometry for all the objects in a field of view.
2. Obtain 2MASS *JHK* photometry in the field of view. This can be downloaded from the GATOR server at the NASA/IPAC Infrared Science Archive.[15]
3. Match the CH_4s, CH_4l, and 2MASS objects. Our implementation of this step was carried out using M. Richmond's MATCH code.[16]
4. Avoiding any known or suspected T dwarfs within the field of view, select matched objects with $-0.05 < (J - H)_{2MASS} < 0.5$ and $0.6 < (J - H)_{2MASS} < 1.1$ and uncertainty in 2MASS magnitude less than 0.1 mag. Then use equations (2) and (3) to estimate the $CH_4s - CH_4l$ for these objects based on their $J - H$ color and derive a first-pass zero-point $CH_4s - CH_4l$ calibration.
5. Repeat this step, further rejecting any objects with $CH_4s - CH_4l < -0.2$ from the first pass.
6. Apply this zero-point calibration to place data on the $CH_4s - CH_4l$ system.

[14] See http://terapix.iap.fr/soft/sextractor/index.html.
[15] Available at http://irsa.ipac.caltech.edu/applications/Gator.
[16] Available at http://spiff.rit.edu/match.

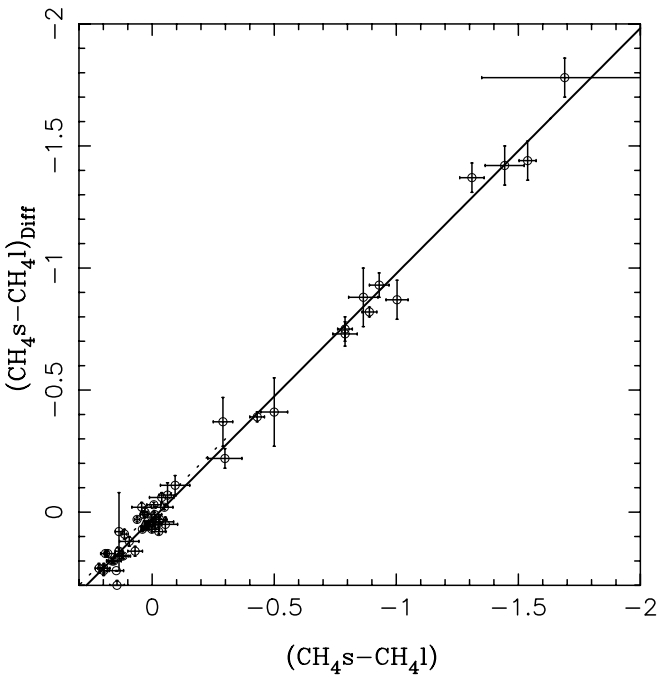

FIG. 6.—$CH_4s - CH_4l$ measurements plotted against $(CH_4s - CH_4l)_{Diff}$ measurements obtained from the same data frames. The dotted line indicates the one-to-one relationship, while the solid line indicates the least-squares fit described in the text. The scatter in $(CH_4s - CH_4l)_{Diff}$ about the fit is 0.05 mag.

We have found that a typical IRIS2 field of view contains between 5 and 15 suitable background objects, leading to zero-point calibrations with a standard error in the mean of <0.05 mag.

Figure 6 shows a plot of the photometry (used to define our methane photometric system in § 2.3) versus differential methane photometry calculated for the same observations using the procedure above. The dotted line shows the one-to-one relationship between the two sets of measurements, while the solid line is a least-squares fit between the two, with the following form:

$$(CH_4s - CH_4l)_{Diff} = 0.029 \pm 0.001 + (1.006 \pm 0.004)(CH_4s - CH_4l). \quad (5)$$

The rms scatter in differential $CH_4s - CH_4l$ about this fit is 0.05 mag. These results indicate that differential $CH_4s - CH_4l$ photometry can be used with confidence at the 0.05 mag level.

2.6. *Methane Imaging Results*

With a typical methane imaging observation consisting of three to five dithered observations in each of the methane filters and exposure times of 30–60 s, a complete WFTS candidate sequence takes ~5 minutes to complete. The ORAC-DR system is able to process these data to publication standard on the fly, and a PERL script automates the processing described in the previous sections, allowing nearly online analysis of each observation during each night (or, at the very latest, on the following afternoon). This has the advantage of allowing almost immediate IRIS2 spectroscopic follow-up of T dwarfs identified by our methane imaging.

To date, we have observed 508 candidate T dwarfs identified as part of the WFTS; of these, 61 revealed no infrared counterpart to the original 2MASS detection, while the remainder were detected in the CH_4s and CH_4l bands. Of these detected objects, 10 have $CH_4s - CH_4l$ colors indicating that they are T dwarfs and have been spectroscopically confirmed as T dwarfs; two

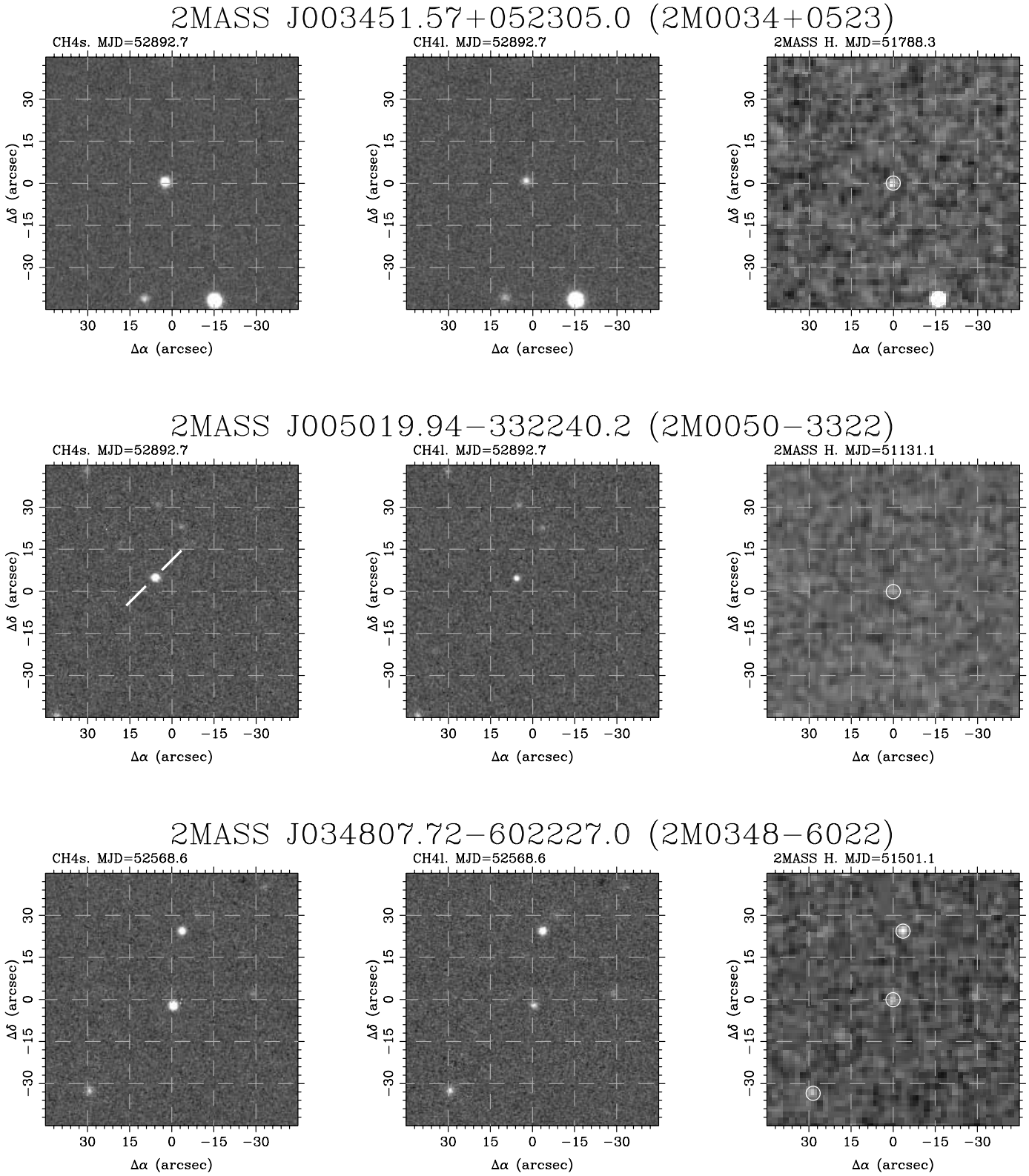

FIG. 7.—Finding charts for WFTS objects listed in Table 4. For each object, images 3′ on a side and centered on the 2MASS Point Source Catalog (PSC) position indicated in CH_4s, CH_4l, and 2MASS *H* are shown. Epochs are indicated by their Modified Julian Dates. Also shown superposed on the *H*-band charts are all the 2MASS PSC sources in each field of view. The WFTS T dwarfs are highlighted in the methane images where proper motions make identification unclear.

have colors suggesting that they may be T dwarfs and have been ruled out by spectroscopy; and three have $CH_4s - CH_4l$ colors suggesting that they may be early T dwarfs and are awaiting spectroscopy to confirm their status. Of the 10 T dwarfs detected by methane imaging from the WFTS, seven (2MASS 0034−33, 1122−35, 1114−26, 0939−24, 0949−15, 1828−48, and 2331−47) were first confirmed as T dwarfs by methane imaging, while a further three were imaged in methane filters after their spectra had been acquired elsewhere (Burgasser et al. 2003c, 2004). Finding charts for all these T dwarfs are shown in Figure 7.

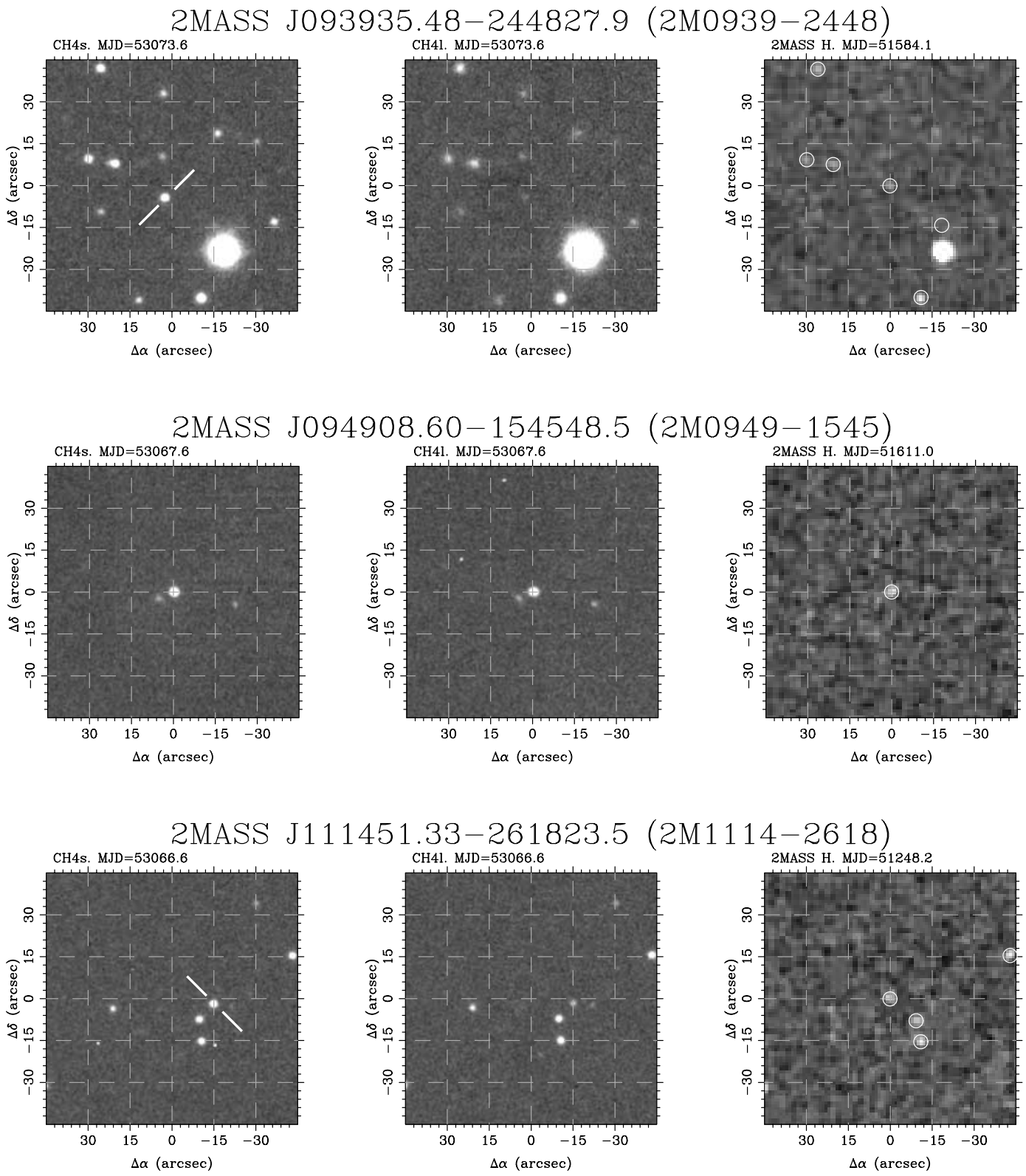

FIG. 7.—*Continued*

Figure 8 summarizes the results of these differential methane observations. It plots $(CH_4s - CH_4l)_{Diff}$ against 2MASS $J-H$ for (1) a sample of known T and L dwarfs; (2) the T dwarfs identified from the WFTS; (3) objects detected by the WFTS methane imaging, but not T dwarfs; (4) a few objects whose methane photometry is not decisive and that need additional spectroscopy to clarify their status; and (5) the "haze" of background objects underlying these data observed in these 508 IRIS2 observations with 2MASS photometric uncertainties <0.05 mag and within $3'$ of the IRIS2 field center. The $CH_4s - CH_4l$ versus $(J-H)_{2MASS}$ sequence of Table 3 is also plotted. The T dwarf differential photometry from this figure is also summarized in Table 4.

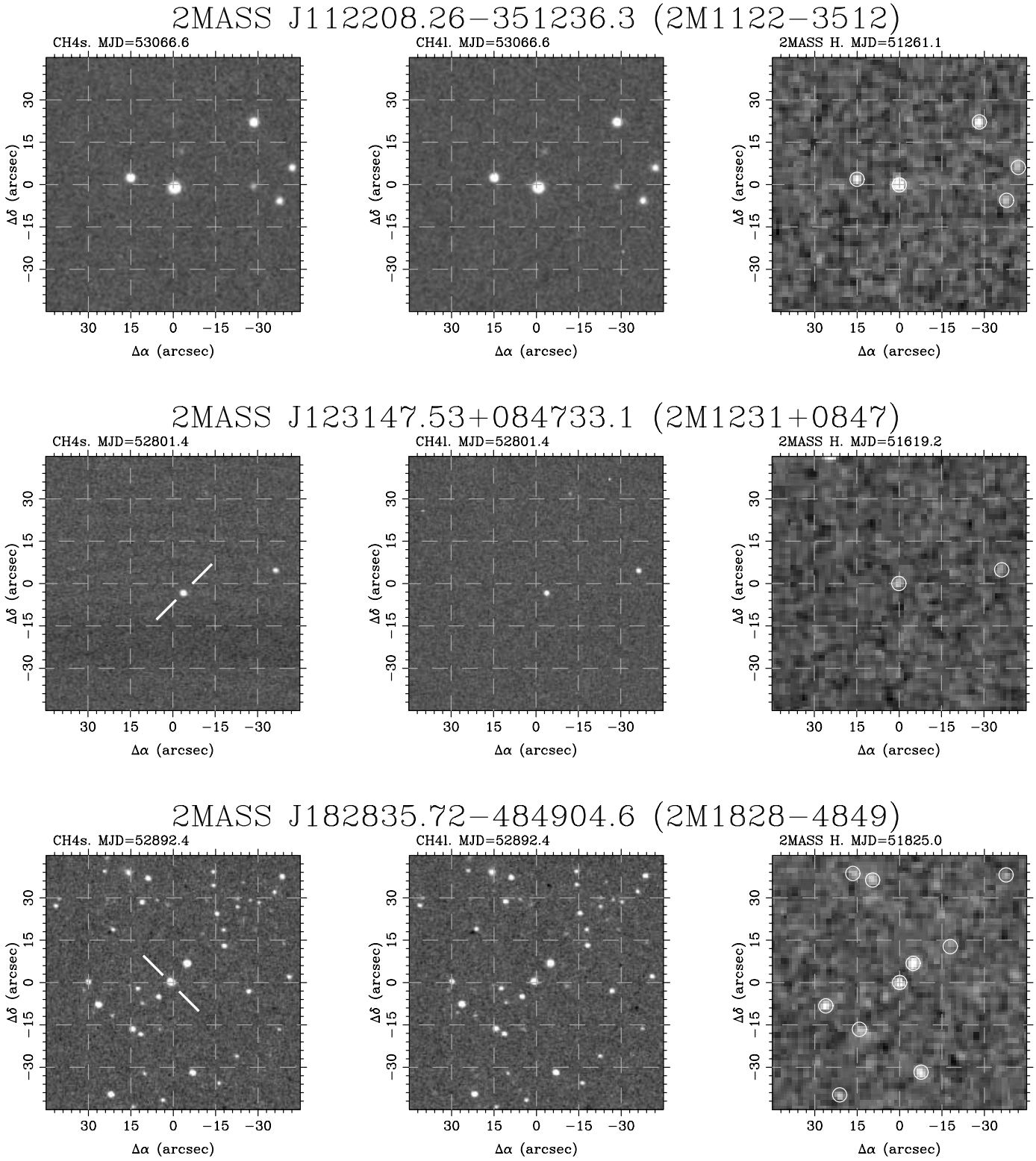

FIG. 7.—*Continued*

These results reinforce the power of methane imaging; we have reduced the need for spectroscopic confirmation from hundreds of objects to 15. It should be noted, however, that while the methane imaging technique is quite clean for late T dwarfs (of the seven WFTS candidates imaged in methane and found to have $CH_4s - CH_4l < -0.5$, all are spectroscopically found to be T dwarfs), it becomes progressively less so for early T dwarfs. (Both "ruled out by spectroscopy" methane candidates have $CH_4s - CH_4l > -0.3$.) For early T dwarfs the large number of background objects with neutral $CH_4s - CH_4l$ colors leads to photometric and differential zero-point uncertainties scattering increasing numbers of background objects into regions where their colors mimic those of early T dwarfs. Similarly, the rate at which T dwarfs could be missed by our methane imaging is a

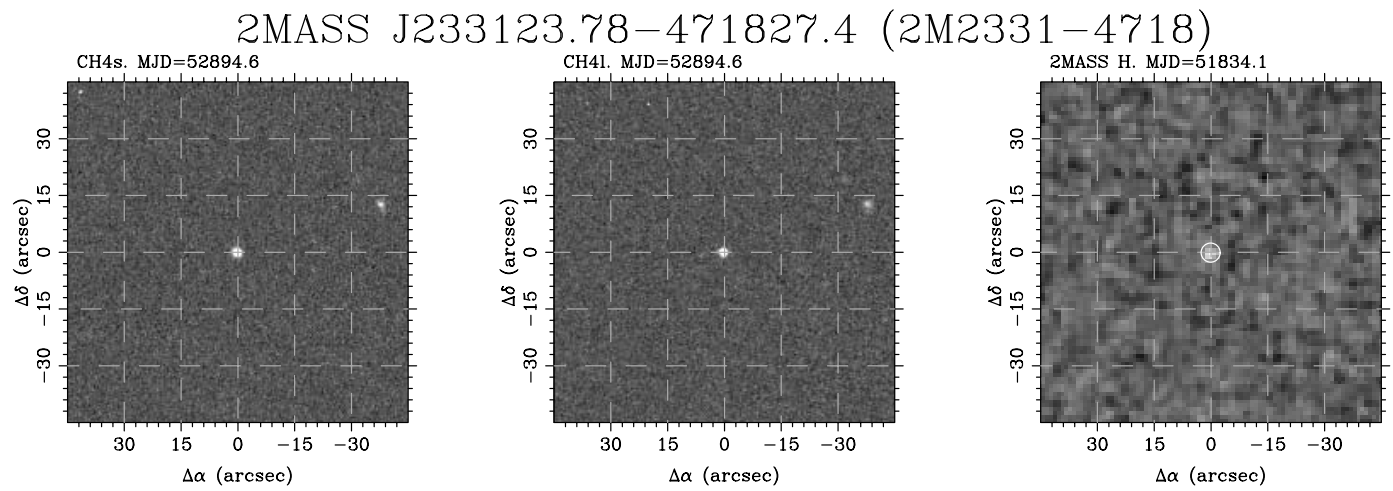

FIG. 7.—*Continued*

strong function of spectral type. As Table 2 indicates, we easily redetect, based on $CH_4s - CH_4l$ color alone, all 11 known T dwarfs later than T4, while for types earlier than T2 position information in addition to $CH_4s - CH_4l$ color is necessary to identify the T dwarf. A detailed analysis of all the WFTS candidates observed (required to examine the efficiency of methane imaging as a function of spectral type and so produce selection functions and luminosity functions from our survey) is postponed to a subsequent paper in which all the WFTS results will be presented and analyzed.

A notable feature of Figure 8 is that the bluest objects in $J - H$ lie systematically below the $CH_4s - CH_4l$–$(J - H)_{2MASS}$ sequence. This is an artifact of the initial color criteria adopted for selection from 2MASS, the 0.1–0.2 mag uncertainties on these colors, and the relative numbers of intrinsically red and blue stars in the 2MASS database. Figure 1 of Burgasser et al. (2003c) shows how the selection used by the WFTS leads to peaks in the number of objects selected at $(J - H)_{2MASS} \approx 0.7$ (equivalent to mid to late-M dwarfs) and $(J - H)_{2MASS} \approx 0.3$ (equivalent to early to mid-G dwarfs). However, M dwarfs hugely outweigh G dwarfs in the 2MASS database, meaning that photometric uncertainties scatter many more actual M dwarfs into the G dwarf peak than there are real G dwarfs in that peak. This is reflected in Figure 8, where we see that most of the objects in the G dwarf

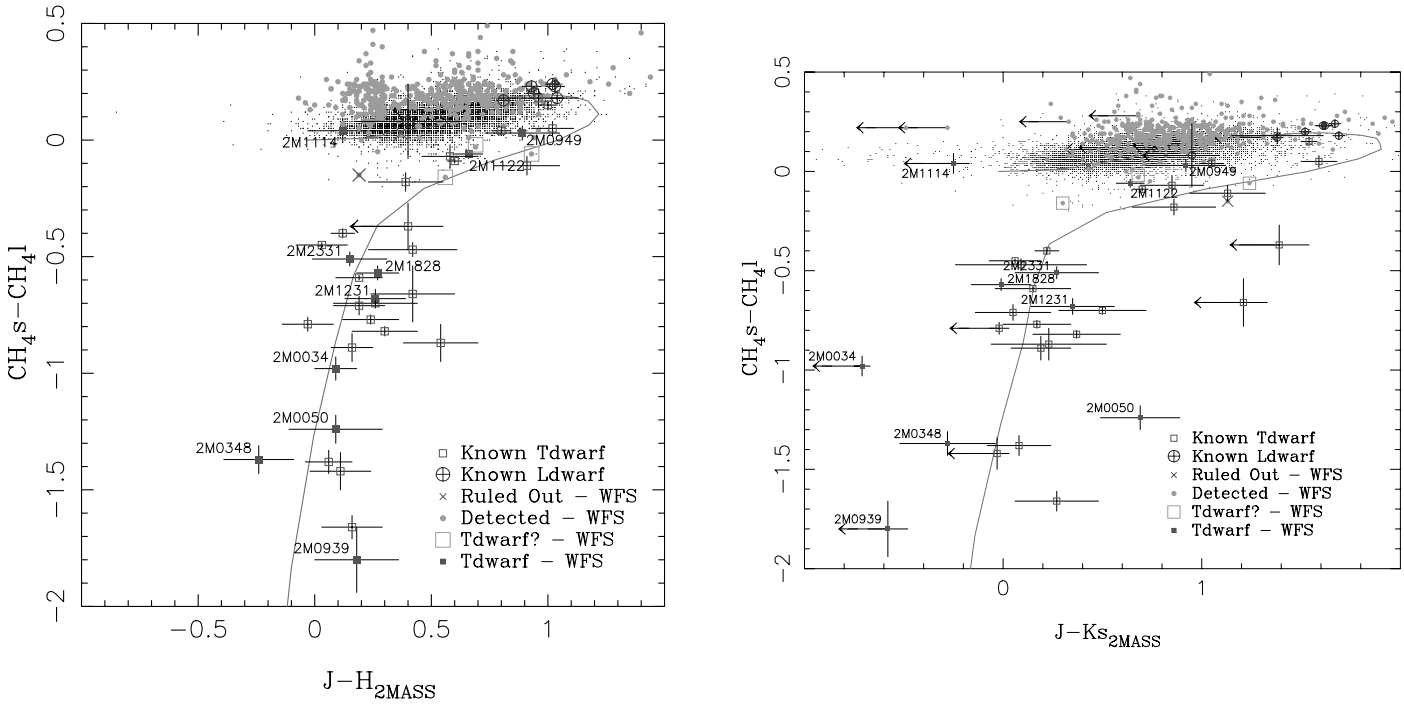

FIG. 8.—$(CH_4s - CH_4l)_{Diff}$ plotted against 2MASS $J - H$ and $J - K_s$ for WFTS candidates observed to date. Objects not detected at K_s or H by 2MASS are indicated as colors with upper limits. WFTS T dwarfs are plotted as filled squares with labels. WFTS objects that were detected but not indicated as being T dwarfs by their $CH_4s - CH_4l$ photometry are plotted as filled circles, objects whose $CH_4s - CH_4l$ photometry suggests a T dwarf status (not yet confirmed by spectra) are highlighted with large open squares, and objects whose spectra have ruled out T dwarf status are overplotted with crosses. Known T dwarfs are shown as open squares (where more than one observation has been taken, they are an average) and known L dwarfs as open circles with crosses. The haze of small points underlying the plot shows all background objects observed during this program within 3′ of the center of the IRIS2 field of view and with 2MASS uncertainties of <0.05 mag. [*See the electronic edition of the Journal for a color version of this figure*.]

TABLE 4

$CH_4s - CH_4l$ Photometry, Proper Motions, and Spectral Types for T Dwarfs

Short Name	Full Name	Spectral Type[a]	CH_4 Spectral Type[b]	$(CH_4s - CH_4l)_{Diff}$[c]	$J - H_{2MASS}$[d]	$H - K_{s2MASS}$[d]	$J - K_{s2MASS}$[d]	μ[e]	θ[e]	References[f]
				WFTS						
2M 0034+0523	2MASS J00345157+0523050	T6.5	T6.5 ± 0.3	−0.98 ± 0.05 (1)	+0.09 ± 0.09	−0.80 ± 0.08	−0.71 ± 0.04:	0.8 ± 0.3	85 ± 15	1
2M 0050−3322.....	2MASS J00501994−3322402	...	T7.1 ± 0.3	−1.24 ± 0.06 (1)	+0.09 ± 0.20	+0.60 ± 0.27	+0.69 ± 0.20	1.5 ± 0.1	53 ± 5	2
2M 0348−6022.....	2MASS J03480772−6022270	T7	T7.4 ± 0.3	−1.37 ± 0.06 (1)	−0.24 ± 0.15	−0.04 ± 0.27	−0.28 ± 0.24	0.76 ± 0.06	196 ± 6	1
2M 0939−2448.....	2MASS J09393548−2448279	...	T8.2 ± 0.3	−1.80 ± 0.14 (1)	+0.18 ± 0.18	−0.76 ± 0.15	−0.58 ± 0.10:	1.15 ± 0.06	155 ± 1	2
2M 0949−1545.....	2MASS J09490860−1545485	...	T0.3 ± 1.5	+0.03 ± 0.03 (2)	+0.89 ± 0.16	+0.04 ± 0.20	+0.92 ± 0.20	0.10 ± 0.04	271 ± 34	2
2M 1114−2618.....	2MASS J11145133−2618235	...	T7.5 ± 0.3	−1.40 ± 0.07 (1)	+0.12 ± 0.15	−0.38 ± 0.12	−0.25 ± 0.08:	3.05 ± 0.04	263.2 ± 0.8	2
2M 1122−3512.....	2MASS J11220826−3512363	...	T1.5 ± 1.1	−0.06 ± 0.02 (1)	+0.66 ± 0.06	−0.02 ± 0.08	+0.64 ± 0.07	0.29 ± 0.03	211 ± 8	2
2M 1231+0847	2MASS J12314753+0847331	T5.5	T5.5 ± 0.4	−0.68 ± 0.04 (1)	+0.26 ± 0.13	+0.09 ± 0.22	+0.35 ± 0.21	1.61 ± 0.07	227 ± 4	1
2M 1828−4849.....	2MASS J18283572−4849046	T5.5	T5.0 ± 0.5	−0.57 ± 0.03 (1)	+0.27 ± 0.09	−0.27 ± 0.16	−0.01 ± 0.15	0.34 ± 0.06	84 ± 10	1
2M 2331−4718.....	2MASS J23312378−4718274	T5	T4.7 ± 0.5	−0.51 ± 0.03 (1)	+0.15 ± 0.16	+0.12 ± 0.25	+0.27 ± 0.21	0.20 ± 0.07	118 ± 6	1
				Other						
SD 0151+1244.....	SDSSp J015141.69+124429.6	T1	L5−T0	+0.18 ± 0.04 (2)	+0.96 ± 0.17	+0.42 ± 0.22	+1.38 ± 0.23	0.90 ± 0.05	100 ± 2	1
SD 0207+0000.....	SDSSp J020742.83+000056.2	T4	T4.0 ± 0.8	−0.37 ± 0.10 (1)	+0.40 ± 0.15	:	+1.39 ± 0.15:	0.30 ± 0.13	101 ± 13	1
2M 0243−2453.....	2MASS J02431371−2453298	T6	T5.8 ± 0.5	−0.77 ± 0.02 (3)	+0.24 ± 0.12	−0.08 ± 0.20	+0.17 ± 0.17	0.28 ± 0.05	229 ± 25	1
2M 0415−0935.....	2MASS J04151954−0935066	T8	T8.0 ± 0.2	−1.66 ± 0.03 (3)	+0.16 ± 0.13	+0.11 ± 0.23	+0.27 ± 0.21	2.31 ± 0.04	76 ± 1	1
SD 0423−0414.....	SDSSp J042348.57−041403.5	T0	L3−T0	+0.15 ± 0.02 (4)	+1.00 ± 0.04	+0.53 ± 0.05	+1.54 ± 0.04	0.29 ± 0.04	281 ± 9	1
2M 0516−0445.....	2MASS J05160945−0445499	T5.5	T5.6 ± 0.3	−0.70 ± 0.02 (3)	+0.26 ± 0.18	+0.23 ± 0.26	+0.50 ± 0.22	0.30 ± 0.04	234 ± 9	3
2M 0559−1404.....	2MASS J05591914−1404488	T4.5	T4.1 ± 0.4	−0.40 ± 0.02 (3)	+0.12 ± 0.05	+0.10 ± 0.07	+0.22 ± 0.06	0.72 ± 0.04	120 ± 1	1
SD 1021−0304.....	SDSSp J102109.69−030420.1	T3.5	T2.3 ± 1.0	−0.11 ± 0.04 (4)	+0.91 ± 0.14	+0.22 ± 0.20	+1.13 ± 0.19	0.17 ± 0.04	252 ± 40	1
SD 1110+0116	SDSSp J111010.01+011613.1	T5.5	T5.5 ± 0.5	−0.66 ± 0.12 (2)	+0.42 ± 0.18	+0.79 ± 0.14	+1.21 ± 0.12:	0.34 ± 0.10	110 ± 27	1
SD 1207+0244.....	SDSSp J120747.17+024424.8	T0.5	T0 ± 1.5	+0.05 ± 0.03 (1)	+1.02 ± 0.09	+0.57 ± 0.09	+1.59 ± 0.09	0.39 ± 0.09	286 ± 13	1
2M 1217−0311.....	2MASS J12171110−0311131	T7	T7.5 ± 0.3	−1.42 ± 0.08 (1)	+0.11 ± 0.13	−0.14 ± 0.12	−0.03 ± 0.06:	1.00 ± 0.06	278 ± 3	1
2M 1225−2739.....	2MASS J12255432−2739476AB	T6	T6.4 ± 0.3	−0.89 ± 0.06 (2)	+0.16 ± 0.09	+0.03 ± 0.17	+0.19 ± 0.15	0.72 ± 0.03	146 ± 1	1
SD 1254−0122.....	SDSSp J125453.90−012247.4	T2	T0.1 ± 1.5	+0.04 ± 0.02 (1)	+0.80 ± 0.04	+0.25 ± 0.06	+1.05 ± 0.06	0.45 ± 0.06	285 ± 6	1
SD 1346−0031.....	SDSSp J134646.45−003150.4	T6.5	T5.8 ± 0.4	−0.87 ± 0.08 (1)	+0.54 ± 0.16	−0.31 ± 0.30	+0.23 ± 0.29	<0.24	...	1
Gl 570d.....	...	T7.5	T7.5 ± 0.2	−1.38 ± 0.05 (4)	+0.06 ± 0.10	+0.03 ± 0.18	+0.08 ± 0.16	1.99 ± 0.03	147.7 ± 0.6	1
2M 1534−2952.....	2MASS J15344984−2952274AB	...	T4.4 ± 0.5	−0.45 ± 0.01 (1)	+0.03 ± 0.11	+0.02 ± 0.15	+0.06 ± 0.13	0.28 ± 0.03	156 ± 3	...
2M 1546−3325.....	2MASS J15462718−3325111	...	T5.1 ± 0.4	−0.59 ± 0.01 (1)	+0.19 ± 0.10	−0.04 ± 0.20	+0.15 ± 0.19	0.25 ± 0.04	38 ± 12	...
SD 1624+0029.....	SDSSp J162414.37+002915.6	T6	T5.9 ± 0.4	−0.79 ± 0.03 (1)	−0.03 ± 0.11	+0.01 ± 0.10	−0.02 ± 0.05:	0.34 ± 0.07	256 ± 18	1
SD 1750+1759.....	SDSSp J175032.96+175903.9	T3	T2.6 ± 0.9	−0.18 ± 0.04 (1)	+0.39 ± 0.16	+0.47 ± 0.23	+0.86 ± 0.21	0.22 ± 0.08	100 ± 12	1
ϵ Ind BC.....	...	...	T1.7 ± 1.0	−0.09 ± 0.01 (3)	+0.60 ± 0.03	+0.10 ± 0.03	+0.70 ± 0.03	4.74 ± 0.02	120.6 ± 0.2	...
2M 2228−4310.....	2MASS J22282889−4310262	T6	T6.0 ± 0.4	−0.82 ± 0.02 (1)	+0.30 ± 0.14	+0.07 ± 0.24	+0.37 ± 0.22	0.35 ± 0.05	164 ± 5	1
2M 2339+1352	2MASS J23391025+1352284	T5	T4.6 ± 0.4	−0.47 ± 0.03 (2)	+0.42 ± 0.19	−0.32 ± 0.34	+0.09 ± 0.33	1.12 ± 0.20	156 ± 4	1
2M 2356−1553.....	2MASS J23565477−1553111	T5.5	T5.7 ± 0.3	−0.71 ± 0.04 (4)	+0.19 ± 0.11	−0.14 ± 0.21	+0.05 ± 0.19	0.77 ± 0.04	211 ± 7	1

[a] Spectroscopic spectral type.

[b] Methane spectral type, derived from $(CH_4s - CH_4l)_{Diff}$ and eq. (2).

[c] See § 2.5 for the definition of $(CH_4s - CH_4l)_{Diff}$. The number of observations averaged to produce the measurement listed is indicated in parentheses.

[d] $J - H$, $H - K_s$, and $J - K_s$ on the 2MASS photometric system. A colon indicates that the object was not detected in the 2MASS K_s band, and that a 95% confidence upper limit has been used to derive the color, the quoted uncertainty of which is due only to the J detection. SD 0207+0000 was not detected in H or K_s by 2MASS.

[e] Proper-motion magnitude (μ in arcsec yr^{-1}) and direction (θ in degrees east of north). Many of the T dwarfs listed in the table are at distances of 7–20 pc and have annual parallax motions of 0.″125–0.″05, which we have not attempted to control. These introduce proper-motion uncertainties of a magnitude similar to those due to the precision of the astrometric transformation between the two epochs.

[f] If no spectral type is listed for a T dwarf, then no hybrid spectral type has been published or could be calculated from available archival data.

References.—(1) Burgasser et al. 2005; (2) Leggett et al. 2002, Knapp et al. 2004, and Burgasser et al. 2003b, 2003c, 2004 classified using the procedure described in § 3.2; (3) IRIS2 spectral types as described in § 3.2.

TABLE 5
IRIS2 Spectroscopic Observing Adopted

Night	Object	Formats[a]	Exposures (s)	Seeing (arcsec)
2004 Jan 8.....	2M 0050−3322	Jl, H	4 × 600, 4 × 600	1.5
2004 Jan 8.....	SD 0423−0114	Jl, H	4 × 300, 4 × 300	1.9
2004 Jan 8.....	2M 0559−1404	Jl, H	4 × 300, 4 × 300	2.0
2004 Mar 3	2M 1114−2618	Jl, Hs	4 × 600, 4 × 600	2.4
2004 Mar 4	2M 1122−3512	Jl, Hs	4 × 300, 4 × 300	1.9
2004 Mar 4	2M 1114−2618	Jl, Hs	4 × 300, 4 × 300	1.7
2004 Mar 8	2M 0949−1545	Jl, Hs	2 × 600, 2 × 600	2.4
2004 Mar 9	2M 0939−2448	Hs	2 × 600	2.2

[a] See § 3.1 for wavelength coverage and resolutions of these formats.

peak at $(J - H)_{2MASS} \approx 0.3$ have $CH_4s - CH_4l$ color appropriate for M dwarfs, not G dwarfs.

Proper motions have been estimated for all the T dwarfs listed in Table 4. These were calculated by projecting the 2MASS data in each field into a tangent plane centered on the 2MASS target catalog coordinate, using the MATCH code to determine a linear transformation for each astrometrically corrected IRIS2 image to this tangent plane, and estimating the motion between the observation epoch in the 2MASS catalog and the IRIS2 observation epoch. Typical astrometric uncertainties due to this process are in the range 0.″1–0.″2, and typical epoch differences are 4–5 yr. Many of the T dwarfs listed in Table 4 are at distances of 7–20 pc and so have annual parallax motions of 0.″125–0.″05, which we have not attempted to control. These introduce proper-motion uncertainties of a magnitude similar to those due to the precision of the astrometric transformation between the two epochs.

3. SPECTROSCOPY

3.1. *IRIS2 Spectroscopy*

Spectroscopic observations were carried out with IRIS2 on the nights of 2003 July 12–14, 2004 January 8, and 2004 March 3–9 (UT). The targets observed are summarized in Table 5. Observations were obtained with a 1″ slit (corresponding to 2.2 pixels on the detector) in one of three configurations:

1. Jl (Jlong), a 240 line mm^{-1} transmission grating bonded to a sapphire prism ("Sapphire240") used in the collimated beam of IRIS2, together with a spectroscopic blocking filter (which transmits $\lambda = 1100–1350$ nm) to deliver 0.232 nm $pixel^{-1}$ spectra over the wavelength range 1105.2–1343.4 nm on the detector, with a resolution of 2.3 pixels, corresponding to $\lambda/\Delta\lambda = R \approx 2290–2250$.
2. Hs (Hspect), a 316 line mm^{-1} transmission grating bonded to a sapphire prism ("Sapphire316") used with a spectroscopic blocking filter (which transmits $\lambda = 1443–1824$ nm) to deliver 0.346 nm $pixel^{-1}$ spectra over the wavelength range 1485–1795 nm (this wavelength range being primarily determined by terrestrial water vapor transmission), with a resolution of 2.3 pixels, corresponding to $\lambda/\Delta\lambda = R \approx 2050–2150$.
3. H, the same configuration as Hs but with the MKO *H* filter used as a spectroscopic blocker. In this mode, the filter bandpass ($\lambda = 1485–1795$ nm) sets the spectral format recorded (which is nonetheless very similar to that delivered by Hs).

Wavelength calibrations were obtained with a Xe lamp, which enables a third-order polynomial dispersion fit to be obtained with rms scatter about the fit of better than 1/20 of a pixel.

The spectra were acquired by nodding the telescope between two beams ("A" and "B") in either AB or ABBA combinations with observations at each beam of 300–600 s. For spectroscopic observing the detector was operated in multiple read mode, with typically 60 nondestructive reads being acquired over the course of the exposure and the final image being obtained from a least-squares fit to each pixel. This mode delivers an effective read noise in the final image of less than five electrons.

Data reduction followed a more or less standard procedure for infrared spectrographs. The first step for all images was to create a Poisson uncertainty image based on the known gain, read noise, and dark current of IRIS2. The astrometric distortion present in IRIS2 images (see above) delivers spectra with significant curvature (i.e., arc and sky lines are curved on the IRIS2 focal plane). For each spectroscopic configuration, arc lines were used

TABLE 6
Spectroscopic Comparison Objects

Spectral Type	Object
L0	2MASS J03454316+2540233
L0.5	2MASS J07464256+2000321
L3	DENIS-P J1058.7−1548, 2MASS J15074769−1627386
L3.5	2MASS J00361617+1821104
L4.5	2MASS J00283943+1501418, 2MASS J22244381−0158521
L5	DENIS-P J1228.2−1547AB
L6.5	2MASS J22443167+2043433
L7	DENIS-P J0205.4−1159
L7.5	2MASS J08251968+2115521
L8	2MASS J03105986+1648155, 2MASS J03284265+2302051
L8	2MASS J15232263+3014562, 2MASS J16322911+1904407
T0	SDSSp J042348.57−041403.5
T1	SDSSp J015141.69+124429.6
T2	SDSSp J125453.90−012247.4
T3	2MASS J12095613−1004008
T4	2MASS J22541892+3123498
T5	2MASS J15031961+2525196
T6	SDSSp J162414.37+002915.6
T7	2MASS J07271824+1710012
T8	2MASS J04151954−0935066

Note.—Types are from Kirkpatrick et al. (2000) for L dwarfs and Burgasser et al. (2005) for T dwarfs.

TABLE 7
SPECTROSCOPIC SPECTRAL TYPING RESULTS

Object	H_2O^J	CH_4^J	H_2O^H	CH_4^H	$\langle SpT_{spec} \rangle$	SpT_{hyb}	$\langle SpT_{CH_4} \rangle$
SD 0423−0114.....	0.63 ± 0.04	0.93 ± 0.03	...	0.92 ± 0.05	T0.5 ± 1.0	T0	L3–T0
2M 0949−1545.....	0.68 ± 0.04	0.94 ± 0.03	0.60 ± 0.03	0.72 ± 0.05	T1.0 ± 1.0	...	T0.3 ± 1.5
2M 1122−3512.....	0.55 ± 0.04	0.89 ± 0.04	0.51 ± 0.03	0.71 ± 0.05	T2.0 ± 0.5	...	T1.5 ± 1.1
2M 0559−1404.....	0.36 ± 0.04	0.79 ± 0.04	...	0.44 ± 0.05	T4.5 ± 0.5	T4.5	T4.1 ± 0.4
2M 0050−3322.....	0.08 ± 0.04	0.46 ± 0.04	...	0.14 ± 0.05	T7.5 ± 0.5	...	T7.1 ± 0.3
2M 1114−2618.....	0.03 ± 0.04	0.38 ± 0.04	0.18 ± 0.03	0.13 ± 0.05	T7.5 ± 0.5	...	T7.5 ± 0.3
2M 0939−2448.....	...	...	0.14 ± 0.03	0.13 ± 0.05	T8.0 ± 0.5	...	T8.2 ± 0.3

to construct a correction that removes this curvature using the Figaro *sdist* and *cdist* codes. These were applied to flat-field images (obtained by subtracting images of the AAT dome obtained when illuminated with a quartz halogen lamp from images obtained with the lamp turned off) to produce a "straightened" flat-field image. The spectral response of this flat field was then determined by collapsing this image in the spatial direction and making a smooth spline fit through it. By then growing this smooth spectral response into an image and reversing the distortion correction, we obtained an image that could normalize the raw flat-field images and provide a true pixel-to-pixel spectroscopic flat field.

All images were flattened with these flat fields and then sky-subtracted with the relevant exposures in the AB or ABBA observing pattern. The IRIS2 astrometric distortion was then removed, delivering spectra with constant wavelength at all columns on the detector, with the majority of the sky lines subtracted (although changes in the strength of the near-infrared night sky lines always result in some residual differences being present in these sky-subtracted images). The tilt of the dispersed spectra relative to the detector rows ($<0.^{\circ}5$) was then removed.

The observed targets were identified in these processed images and used to define windows for a further sky-subtraction pass (by fitting along the columns of the detector), followed by flagging of cosmic rays by hand and then optimal extraction. At each step of this process, the initial photon-counting errors were propagated, so that the final result was a spectrum with meaningful uncertainties. Wavelength calibration was obtained by passing Xe arc lamp images through the same process and extracting them from the same detector regions as each object.

The same procedures were used to reduce observations of A, F, and G stars obtained either immediately before or immediately after our target star, in the same instrument configurations. These were used to correct the effects of terrestrial atmospheric absorption for each target, assuming a blackbody flux distribution for each terrestrial correction star based on its spectral type. The strong hydrogen absorption lines in the *H*-band spectra of A-type stars were found to make them essentially useless for this purpose, so these spectra were discarded. These terrestrial correction stars not only enabled us to remove the effects of atmospheric absorption but also to place our final spectra on a meaningful F_λ flux scale, although with arbitrary zero-point calibration uncertainty due to the slit losses when observing the terrestrial calibration star.

For purposes of spectral typing, the main features of interest are broad, so we have binned our spectra from their full $R \approx 2200$ resolution to $R \approx 370$ (i.e., binned by a factor of 6). The binning weighted each pixel by the inverse square of its uncertainty, resulting in pixels lying on strong night sky lines receiving low weight in the final binning—effectively, "software night sky suppression." Tests with our spectra show that this procedure can deliver spectra with a given signal-to-noise ratio with an efficiency about 1.4–1.7 times faster than is possible by simply observing at $R \approx 370$.

3.2. *Analysis*

To place our spectra in a spectral-typing sequence (and to derive uniform types for all the T dwarfs observed in our methane filters), we numerically quantify their large-scale appearance using near-infrared spectroscopic indices. Numerous authors (following the initial work of Jones et al. [1994, 1996]) have shown that near-infrared spectra offer multiple features that can be used to classify ultracool dwarfs. The use of near-infrared spectroscopic indices to quantify the strength of broad molecular features in ultracool dwarfs was pioneered by Delfosse et al. (1997; see also Tinney et al. 1998; Delfosse et al. 1999) and has since been extended throughout the M and L spectral types by

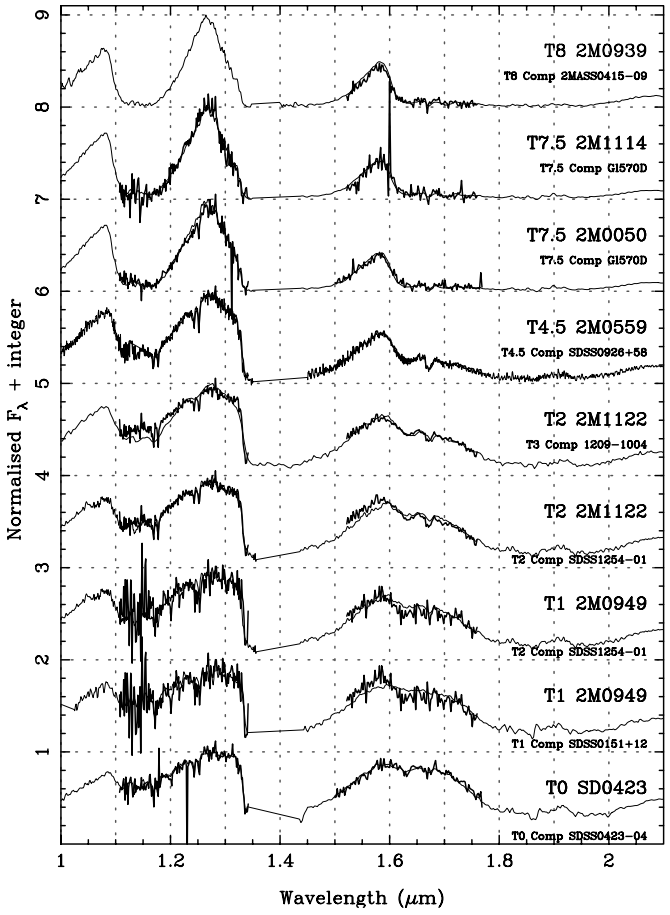

FIG. 9.—IRIS2 T dwarf spectra (*thick lines*) overplotted on T dwarf comparison spectra (*thin lines*; see § 3.2). The spectral types assigned to the IRIS2 spectra are from Table 7. The adopted comparison spectral types are from the final hybrid classification scheme of Burgasser et al. (2005).

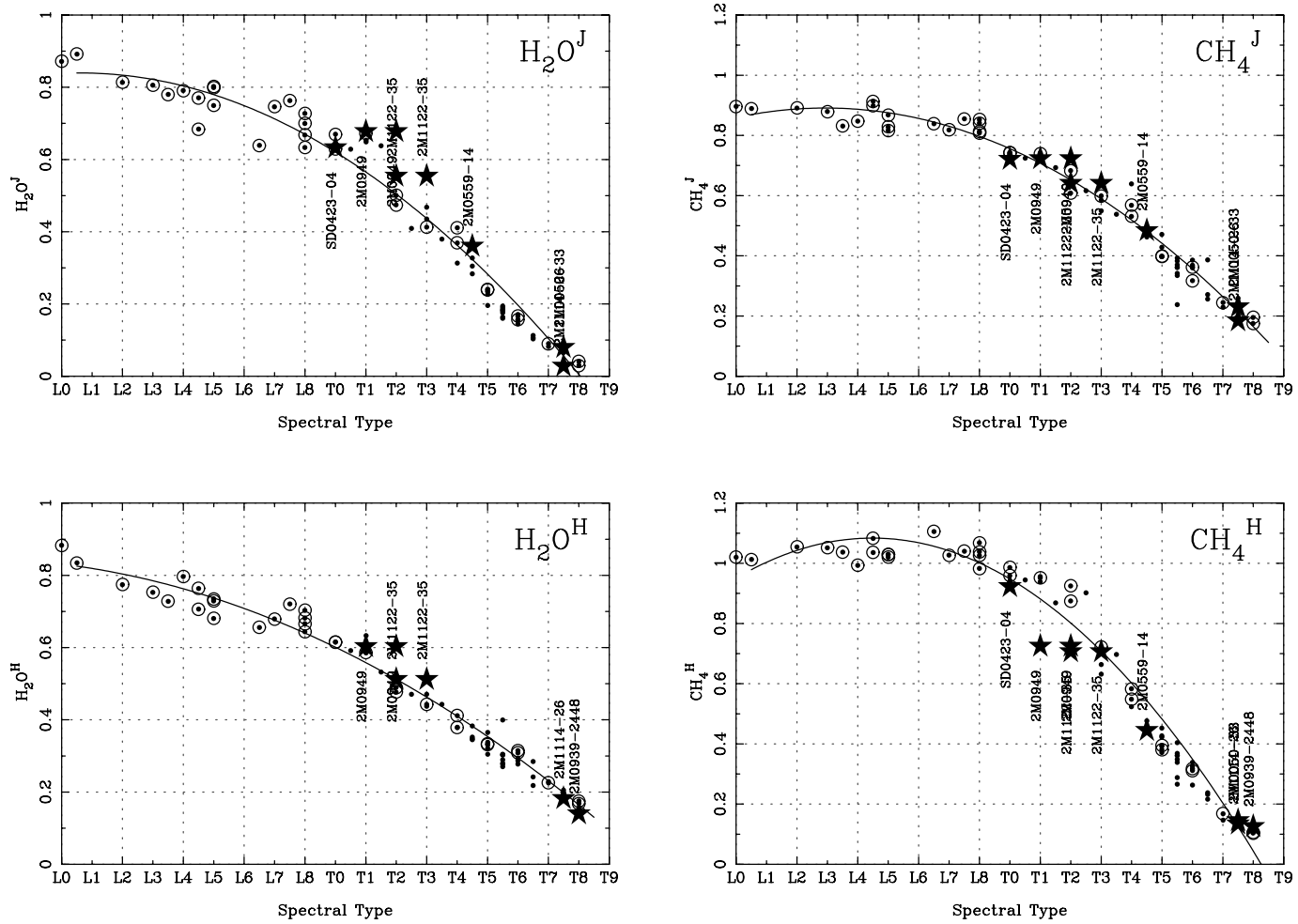

FIG. 10.—Spectroscopic classification indices for both our fundamental calibration objects (*filled circles inside open circles*), other known T dwarfs with hybrid T types (*filled circles*), and objects observed with IRIS2 (*stars*).

Reid et al. (2001), who used the optical M and L dwarf spectral classification system of Kirkpatrick et al. (2000) as their fundamental standards and derived calibrations to transfer infrared spectral indices onto these optical L types. Testi et al. (2001) have continued in this vein for a sample of L dwarfs observed in the near-infrared at very low resolution. For T dwarfs, near-infrared spectra *define* the spectral type. Two separate infrared-typing schemes were initially developed by Burgasser et al. (2002) and Geballe et al. (2002) (the latter including a near-infrared classification of L dwarfs). Both are based on spectroscopic indices that are sensitive to the strength of H_2O and CH_4 molecular absorption. A hybrid scheme was proposed by Burgasser et al. (2003a) to bring these two schemes into alignment. Preliminary spectral indices and spectroscopic standards for this hybrid scheme were presented by Burgasser et al. (2004); the final version of this scheme is imminent (Burgasser et al. 2005).

To classify the T dwarfs identified by methane-band imaging, we used the H_2O^J, CH_4^J, H_2O^H, and CH_4^H indices of Burgasser et al. (2005). (These are the same as those in Burgasser et al. [2004] but with the numerator of the CH_4^J index shifted redward by 0.015 μm.) We have used publicly available L dwarf (Knapp et al. 2004)[17] and T dwarf[18] spectra to calibrate these indices (Table 6). These are monotonic in the H_2O indices for L and T dwarfs and in the CH_4 indices for objects later than L6. They therefore enable a spectral type to be estimated from each index for each T dwarf, with the final spectral type being adopted as the mean of these values (rounded to the nearest half-subtype).

These indices and the derived spectral types are summarized in Table 7 for the T dwarfs observed with IRIS2. The uncertainties listed on these types are the standard error in the mean. These types were then used to order our spectra in a sequence with comparison spectra—both our spectra (*thick lines*) and comparison spectra (*thin lines*) are shown in Figure 9—each segment of the IRIS2 spectrum being normalized to the comparison spectrum on which it is plotted. The spectra classifications derived are consistent between the *H*- and *J*-band spectra for all the new T dwarfs, except for 2MASS 0949−1545 and 1122−3512. For these objects the spectral types indicated by the *H*-band spectra are somewhat later than those indicated by the *J*-band spectra. This could be due to the effects of unresolved binarity or to an underlying structure in the CH_4^H index calibration, which is not adequately parameterized by the polynomial fits shown in Figure 10. In either case, the spectral types for these objects should be regarded as somewhat more uncertain than those for the other T dwarfs presented.

4. DISCUSSION

4.1. *The New T Dwarfs*

Five of the WFTS T dwarfs reported in Table 4 (2MASS 0050−3322, 0939−2448, 0949−1545, 1114−2618, and 1122−3512)

[17] Available at http://www.jach.hawaii.edu/~skl/LTdata.html.
[18] Available at http://research.amnh.org/~adam/tdwarf.

TABLE 8
Distance and Tangential Velocity Estimates for WFTS T Dwarfs

Object Name	Spectral Type[a]	2MASS J	d[b] (pc)	V_{tan}[c] (km s^{-1})
2M 0034+0523	T6.5	15.54 ± 0.04	9	37 ± 19
2M 0050−3322.....	T7.5	15.93 ± 0.07	8	55 ± 13
2M 0348−6022.....	T7	15.32 ± 0.05	7	24 ± 6
2M 0939−2448.....	T8	15.98 ± 0.10	8	46 ± 8
2M 0949−1545.....	T1	16.15 ± 0.12	20	10 ± 6
2M 1114−2618.....	T7.5	15.86 ± 0.08	7	109 ± 20
2M 1122−3512.....	T2	15.02 ± 0.04	14	19 ± 5
2M 1231+0847	T5.5	15.57 ± 0.07	15	114 ± 24
2M 1828−4849.....	T5.5	15.18 ± 0.05	12	21 ± 7
2M 2331−4718.....	T5	15.66 ± 0.07	18	18 ± 9

[a] Spectroscopic spectral type from Table 7 where IRIS2 spectra are available and Table 4 otherwise.
[b] Distance estimate using the 2MASS J absolute magnitude vs. spectral type relation of Tinney et al. (2003) resulting in typical distance uncertainties of ±20%.
[c] Uncertainty includes 0.36 mag scatter about absolute magnitude–spectral type relation and photometric uncertainties for each T dwarf.

are reported for the first time in this paper. A further four objects (2MASS 0034+0523, 1231+0847, 1828−4849, and 2331−4718) were confirmed as T dwarfs by our methane imaging in parallel with the traditional spectroscopic approach and have already been published by Burgasser et al. (2004). Three of the five new T dwarfs (2MASS 0050−3322, 1114−2618, and 0939−2448) are very cool objects with spectral types of T7.5 or later. In comparison, the other two objects are very early; at T1 (2MASS 0949−1545) and T2 (2MASS 1122−3512), they are the earliest T dwarfs yet found by selection for T dwarfs from the 2MASS database.

Of the WFTS T dwarfs reported here, 2MASS 0939−2448 shows pronounced evidence in Figure 8 for the same K-suppressed spectrum previously seen in 2MASS 0034+0523 (Burgasser et al. 2004) and 2MASS 0937+2931 (Burgasser et al. 2002); both 2MASS 0939−2448 and 0034+0523 stand out as having the bluest $J - K_s$ colors of any of the T dwarfs plotted (and, indeed, being only upper limits at K_s in 2MASS). Their $J - H$ colors, by contrast, are not anomalous in any way whatsoever. Note that the anomalously red $J - K_s$ colors of SDSS 0207+0000 and 1110+0116 are not physical but reflect the upper limits of K-band detection from 2MASS of these faint SDSS-discovered objects. On the other hand, 2MASS 0050−3322 does seem to be anomalously red for its methane index. A detailed discussion of the possible causes of K-band flux suppression in T dwarfs is postponed to a forthcoming paper.

Spectrophotometric distance estimates have been derived using the 2MASS J absolute magnitude versus spectral type relation of Tinney et al. (2003). These result in typical distance uncertainties of ±20% and are presented in Table 8. They place all these WFTS T dwarfs at distances of between 5 and 20 pc, making them all likely members of the important and well-studied "Nearby Star" volume-limited sample of objects within 25 pc of the Sun. They are all ideal targets for a 4 m class telescope near-infrared parallax program, and we initiated such a program with IRIS2 on the AAT in 2004. Of these T dwarfs, two (2MASS 1114−2618 and 1231+0847) show appreciable proper motions, indicating tangential velocities of $\gtrsim$100 km s^{-1}.

4.2. *Applications of Methane Imaging*

As outlined in § 1, methane imaging offers significant advantages over current techniques for the identification and classification of T dwarfs. We have shown that this is particularly true for winnowing these rare objects from a large database like 2MASS, for which we could use methane imaging in place of the combination of infrared imaging plus optical imaging plus infrared spectroscopy previously employed. Moreover, the greatly simplified data processing allows almost instantaneous feedback and spectroscopic confirmation, if necessary.

4.2.1. *Large Survey Winnowing*

Perhaps the most obvious application for methane imaging is the winnowing of forthcoming large surveys for cool brown dwarfs. The UKIDSS (Hambly et al. 2003), for example, will carry out surveys in the Y, J, H, and K passbands totaling a volume sensitivity for cool brown dwarfs almost 250 times larger than that obtained by 2MASS. While the filters used in these surveys will be far more suitable for the selection of cool brown dwarfs than those used by 2MASS (Leggett et al. 2005), it is nonetheless true that T dwarfs in the UKIDSS will represent a similar, tiny fraction of the total number of sources ($\lesssim 3 \times 10^{-5}$) to that seen in 2MASS. Hard-won experience shows that when selecting objects this rare from a large database, the resulting sample is *always* dominated by contaminants: detector artifacts, ghosts, asteroids, cosmic rays, partially resolved binaries, confused sources near the survey limits, etc. Such contaminants produce catalog sources with arbitrarily odd colors, some of which will mimic T dwarfs. The class of brown dwarfs cooler than T dwarfs (tentatively known as the "Y" dwarfs, and one of the key science drivers for the UKIDSS) will be even rarer, and candidate samples will be subject to even more contamination. Models for these objects suggest that they will have extremely unusual colors and will lie some way from the sequence of foreground and background G–M dwarfs in a $J - H$ versus $Y - J$ color-color diagram—as much as a magnitude redder in $Y - J$ and a magnitude bluer in $J - H$. The ±0.1–0.2 mag photometric uncertainties of objects near the survey magnitude limits will only rarely scatter G–M dwarfs by the 5–10 σ needed to move such objects into the Y dwarf selection region. But this will only need to happen at a rate of one in a billion to still massively outnumber the likely number of true Y dwarfs in the survey.

Some form of winnowing of candidates is almost inevitably going to be required before taking $H \approx 18$ Y dwarf candidates to an 8 m telescope for infrared spectroscopy. Methane imaging offers an ideal mechanism for doing this, since $H \approx 18$ can be imaged on a 4 m telescope in under an hour, compared to the several hours required to acquire spectra on an 8 m telescope.

4.2.2. *Cluster T Dwarfs*

It has been a commonplace among astronomers for many years that there must exist a minimum mass for star formation, below which the mass function turns over. Based initially on Jeans mass arguments (Low & Lynden-Bell 1976) and later on hydrodynamic simulations (Boss 1988, 1992), this minimum mass was placed at $\sim$0.01 $M_\odot$ (or $\sim 10 M_J$). The similarity of this value to the minimum mass for deuterium burning at $\sim 13 M_J$ has led to a (10–13)M_J value being widely assumed as the minimum mass for star formation (or the maximum mass for planet formation)[19] and so as a dividing line between stars and planets. Below this mass, compact astrophysical objects are assumed to form within planetary disks via the "bottom-up" processes of

[19] See http://www.ciw.edu/boss/IAU/div3/wgesp/definition.html.

planetary accretion. Unfortunately, this comforting paradigm has become somewhat more confused of late.

1. Boss (2001) has included some magnetic field effects in simulations that show that star formation processes can make compact objects as small as $1M_J$.

2. Candidate objects with masses that theoretical models suggest have masses similar to and smaller than $10M_J$ are being turned up by surveys in star-forming regions in an apparent extension of "star" formation to "planetary" masses. These potentially "unbound" planets represent a challenge and a conundrum for the simple paradigm above—are they brown dwarfs formed via star formation processes, stellar embryos ejected from multiple systems before they can accrete sufficient matter to become stars (Reipurth & Clarke 2001), or giant planets ejected from their host stars?

3. Measurements of the brown dwarf mass function in a variety of moderate-age clusters (>100 Myr) are finding results in the range $\propto m^{-0.5}$ to $\propto m^{-0.6}$ (Bouvier et al. 2003), suggesting a mass function that is continuous with the stellar function but continues to turn over at lower and lower masses, extending into the T dwarf range in some clusters.

4. Radial velocity programs are now detecting more massive analogs (extending up to $15M_J$) of the $m \sin i = (0.1\text{–}5)M_J$ exoplanets. The mass function of these exoplanets is consistent with a single power law $\propto (m \sin i)^{-0.8}$ or steeper (Marcy et al. 2004). This is steeper again than the cluster brown dwarf mass function.

There is a need to clarify the status of the mass function in the range in which the lines between planets and brown dwarfs are so blurred. Determining the relative normalizations between the two mass functions is essentially impossible; however, we can attempt to address the *shape* of the mass function in this boundary region. That is, we can try to answer the question, Does the star formation mass function turn over between $40M_J$ and $5M_J$? If it does, then we must determine where it does, as this is critical information needed to refine models of the star formation process.

Unfortunately, while sky surveys have been extremely successful at detecting field brown dwarfs, their unknown ages make the measurement of masses problematic. Such studies need to target stellar clusters of known age in order to estimate masses. Unfortunately, clusters close enough to the Sun for brown dwarfs to be detectable are large on the sky (typically 0.2–10 deg^2) and typically show low contrast against the low-latitude background of field stars. Moreover, the photospheres of cool brown dwarfs are phenomenally complex, leading to real difficulties for theoretical models. This makes traditional color-magnitude diagrams a poor means of selecting cluster members, because uncertainties force the selection of very large samples in color-magnitude space, with poor hit rates for *actual* cluster members. The resulting imaging samples then require substantial spectroscopic winnowing on 8–10 m telescopes.

T dwarf methane absorption, however, is so spectrally unique that it provides a potentially powerful tool for selecting candidate T dwarfs in clusters. Tinney et al. (2003) have looked at the absolute magnitudes at which methane may begin to appear in some representative clusters and concluded that in nearby ($d \approx 150$ pc), 10–20 Myr old clusters such as IC 2391 or IC 2602, the absolute magnitude for CH_4 to become detectable by methane imaging (equivalent to spectral types T2 and later) will be $M_H \sim 12.5$ or, equivalently, $H \sim 18.2$. Later T types will appear at fainter magnitudes, with the more easily detectable levels of methane absorption seen in T5 dwarfs appearing around 1.5 mag fainter.

Using the available T dwarf models (see Tinney et al. [2003] and references therein), we can estimate the second-order *differential* corrections to this first-order methane onset estimate. If we adopt the absolute magnitude corresponding to an easily detectable spectral type of T5 as our measure (hereafter $M^{T5}_{CH_4}$), we can estimate offsets from the $M^{T5}_{CH_4} \approx 14$ of field dwarfs to the $M^{T5}_{CH_4}$ for younger clusters, as well as the masses to which these $M^{T5}_{CH_4}$ values correspond. For clusters of age 100, 50, 10, and 5 Myr the relevant offsets are found to be, respectively, $\Delta M^{T5}_{CH_4} = -0.7, -1.0, -1.3$, and -1.5, and the masses to which these $M^{T5}_{CH_4}$ values correspond are 0.02, 0.012, 0.008, and 0.006 $M_\odot$. For any given cluster, therefore, a survey can be designed using CH_4 selection to probe mass functions at unprecedentedly low masses. As an example, the IRIS2 imager is able to detect T5 dwarfs in the IC 2391 cluster ($d = 140$ pc, age $= 20 \pm 10$ Myr) after just 8 hr of integration (i.e., 4 hr in each bandpass), reaching to a depth of $H = 21$ over an area of 64 arcmin^2, corresponding to a detection threshold mass of $\approx 10M_J$.

The resulting T dwarf imaging candidates will still need to be followed up spectroscopically, in order to distinguish young cluster members from old field T dwarf contaminants. But it is nonetheless true that contamination by non–T dwarfs can be arranged to be small or negligible, vastly improving the speed of confirmation or rejection of cluster membership for T dwarfs.

4.2.3. *Cool Companions to Known Brown Dwarfs*

Very rare astronomical objects (such as T and Y dwarfs) are typically searched for by surveying very large chunks of the sky. An alternate approach is to rely on the fact that most astronomical objects are clustered and therefore to search for rare objects in the vicinity of objects of a similar nature. It was exactly such a search technique that revealed the first T dwarf, Gl 229B (Nakajima et al. 1995). The invariable difficulty in such searches is telling the difference between a potentially interesting companion to the target in question and the vast majority of background objects. In the case of Gl 229B, the companion was revealed by its common proper motion. Methane imaging offers a potentially powerful way to identify cool companions to nearby stars and brown dwarfs without the need to wait for the year or more needed to confirm or deny common proper motion. For example, a few hours of integration with the methane filters in IRIS2 can easily reach to sensitivities adequate to detect methane absorption in objects 3–4 mag fainter than all the T dwarfs so far identified from 2MASS, making this a potentially easier way in which to find Y dwarfs than a large blind survey.

4.2.4. *Methane Variability and Weather*

There is now considerable evidence to indicate that many, if not most, brown dwarfs rotate quite rapidly, with either measured (Bailer-Jones & Lamm 2003; Clarke et al. 2002a, 2002b; Enoch et al. 2003; Gelino et al. 2002; Koen 2003; Bailer-Jones & Mundt 2001; Tinney & Tolley 1999) or inferred (Bailer-Jones 2004; Smith et al. 2003; Mohanty & Basri 2003; Reid et al. 2002; Tinney & Reid 1998) rotation timescales of 1–10 hr. L- and T-type brown dwarfs are also well known to suffer greater or lesser degrees of condensate and/or cloud layer formation (see, e.g., Ackerman & Marley 2001; Allard et al. 2001; Burrows & Sharp 1999). Thus, brown dwarfs have the two ingredients required for the existence of complex, rotationally driven weather patterns on their surfaces. Unfortunately, despite much intensive searching (see references above), detailed evidence for weather variations in brown dwarfs remains elusive.

However, as the source of the dominant absorption feature in the spectra of T dwarfs, searches for variability in CH_4 absorption

(reflecting an uneven surface coverage at the optical depths at which these absorptions are formed) could be extremely powerful (Tinney 2000). Jupiter, for example, is known to show strong surface features in the infrared where gaps in its methane layers allow the hotter, lower regions of the photosphere to shine through (see, e.g., the images of Jupiter in Gelino & Marley [2000]). The nearly differential nature of methane imaging should make possible significantly higher precisions (i.e., <0.01 mag) in programs targeting single objects in extended campaigns than have been achieved in this program. In particular, bright T dwarfs can be targeted (or larger telescopes used) to improve photon-counting uncertainties, observation of a single object for variability makes the zero-point uncertainty associated with the selection of an ensemble of background objects moot, and use of the $CH_4s - CH_4l$ color should obviate many of the second-order differential extinction effects discussed by Bailer-Jones & Lamm (2003).

5. CONCLUSION

We have shown that methane filters can be used to efficiently detect and characterize T dwarfs. We have provided a procedure for calibrating methane filter observations onto a CH_4s, CH_4l photometric system using 2MASS photometry as a calibration system. Five new T dwarfs discovered as part of the 2MASS Wide-Field T Dwarf Search using this technique have been presented. Finally, we have discussed potential further uses for these methane filters, including the winnowing of large survey data sets for T and Y dwarfs, the detection of very low mass brown dwarfs (as low as $10M_J$) in nearby star clusters, the detection of cooler companions to already known brown dwarfs, and the detection of variability signatures due to rotating cloud structures in T dwarfs.

The authors wish to gratefully acknowledge the Joint Astronomy Centre, Hawaii, for making their ORAC-DR code available and for assisting the AAO in implementing it for IRIS2. This wonderful data reduction package has *significantly* improved the efficiency with which this observing program was carried out. We would also like to acknowledge Michael Richmond, Emmanuel Bertin, and Tim Pearson, the authors of the MATCH, SExtractor, and PGPLOT codes, which contributed significantly to this work. A. J. B. acknowledges support by the National Aeronautics and Space Administration (NASA) through the SIRTF Fellowship program. J. D. K. acknowledges the support of the Jet Propulsion Laboratory, California Institute of Technology, which is operated under contract with NASA. C. G. T. joins his US colleagues in thanking his employer for paying him. This publication makes use of data from 2MASS, which is a joint project of the University of Massachusetts and the Infrared Processing and Analysis Center (IPAC), funded by NASA and the National Science Foundation. It also makes use of the NASA/IPAC Infrared Science Archive, which is operated by the Jet Propulsion Laboratory, California Institute of Technology, under contract with NASA.

REFERENCES

Ackerman, A. S., & Marley, M. S. 2001, ApJ, 556, 872
Allard, F., Hauschildt, P. H., Alexander, D. R., Tamani, A., & Schweitzer, A. 2001, ApJ, 556, 357
Bailer-Jones, C. A. L. 2004, A&A, 419, 703
Bailer-Jones, C. A. L., & Lamm, M. 2003, MNRAS, 339, 477
Bailer-Jones, C. A. L., & Mundt, R. 2001, A&A, 367, 218
Bertin, E., & Arnouts, S. 1996, A&AS, 117, 393
Bessell, M. S., & Brett, J. M. 1988, PASP, 100, 1134
Boss, A. P. 1988, ApJ, 331, 370
———. 1992, in The Realm of Interacting Binary Stars, ed. J. Sahade, G. E. McCluskey, & Y. Kondo (Dordrecht: Kluwer), 355
———. 2001, ApJ, 551, L167
Bouvier, J., Moraux, E., Stauffer, J. R., Barrado y Navascués, D., & Cuillandre, J.-C. 2003, in IAU Symp. 211, Brown Dwarfs, ed. E. L. Martín (San Francisco: ASP), 147
Burgasser, A. J., Geballe, T. R., Golimowksi, D. A., Leggett, S. K., Kirkpatrick, J. D., Knapp, G. R., & Fan, X. 2003a, in IAU Symp. 211, Brown Dwarfs, ed. E. L. Martín (San Francisco: ASP), 377
Burgasser, A. J., Geballe, T. R., Leggett, S. K., Kirkpatrick, J. D., & Golimowski, D. A. 2005, ApJ, submitted
Burgasser, A. J., Kirkpatrick, J. D., McElwain, M. W., Cutri, R. M., Burgasser, A. J., & Strutskie, M. F. 2003b, AJ, 125, 850
Burgasser, A. J., McElwain, M. W., & Kirkpatrick, J. D. 2003c, AJ, 126, 2487
Burgasser, A. J., McElwain, M. W., Kirkpatrick, J. D., Cruz, K. L., Tinney, C. G., & Reid, I. N. 2004, AJ, 127, 2856
Burgasser, A. J., et al. 2002, ApJ, 564, 421
Burrows, A., & Sharp, C. M. 1999, ApJ, 512, 843
Clarke, F. J., Oppenheimer, B. R., & Tinney, C. G. 2002a, MNRAS, 335, 1158
Clarke, F. J., Tinney, C. G., & Covey, K. R. 2002b, MNRAS, 332, 361
Cutri, R. M., et al. 2003, Explanatory Supplement to the 2MASS All Sky Data Release (Pasadena: Caltech)
Delfosse, X., Tinney, C. G., Forveille, T., Epchtein, N., Borsenberger, J., Fouqué, P., Kimeswenger, S. & Tiphène, D. 1999, A&AS, 135, 41
Delfosse, X., et al. 1997, A&A, 327, L25
Enoch, M. L., Brown, M. E., & Burgasser, A. J. 2003, AJ, 126, 1006
Geballe, T. R., et al. 2002, ApJ, 564, 466
Gelino, C. R., & Marley, M. S. 2000, in ASP Conf. Ser. 212, From Giant Planets to Cool Stars, ed. C. A. Griffith & M. S. Marley (San Francisco: ASP), 322
Gelino, C. R., Marley, M. S., Holtzman, J. A., Ackerman, A. S., & Lodders, K. 2002, ApJ, 577, 433
Gizis, J. E. 2002, ApJ, 575, 484
Golimowski, D. A., et al. 2004, AJ, 128, 1733
Hambly, N., et al. 2003, in IAU Symp. 211, Brown Dwarfs, ed. E. L. Martín (San Francisco: ASP), 477
Hawarden, T. G., Leggett, S. K., Letawsky, M. E., Ballantyne, D. R., & Casali, M. M. 2001, MNRAS, 325, 563
Herbst, T. M., Thompson, D., Fockenbrock, R., Rix, H.-W., & Beckwith, S. V. W. 1999, ApJ, 526, L17
Jones, H. R. A., Longmore, A. J., Allard, F., & Hauschildt, P. H. 1996, MNRAS, 280, 77
Jones, H. R. A., Longmore, A. J., Jameson, R. F., & Mountain, C. M. 1994, MNRAS, 267, 413
Kirkpatrick, J. D., et al. 2000, AJ, 120, 447
Knapp, G. R., et al. 2004, AJ, 127, 3553
Koen, C. 2003, MNRAS, 346, 473
Krist, J. E., Golimowksi, D. A., Schroeder, D. J., & Henry, T. J. 1998, PASP, 110, 1046
Leggett, S. K., Allard, F., Geballe, T. R., Hauschildt, P. H., & Schweitzer, A. 2001, ApJ, 548, 908
Leggett, S. K., et al. 2002, ApJ, 564, 452
———. 2005, in Proc. 13th Cool Stars Workshop, ed. F. Favata et al., in press
Low, C., & Lynden-Bell, D. 1976, MNRAS, 176, 367
Mainzer, A. K., & McLean, I. S. 2003, ApJ, 597, 555
Mainzer, A. K., McLean, I. S., Sievers, J. L., & Young, E. T. 2004, ApJ, 604, 832
Marcy, G., Butler, R. P., Vogt, S. S., & Fischer, D. A. 2004, in IAU Symp. 213, Bioastronomy 2002: Life Among the Stars, ed. R. P. Norris & F. H. Stootman (San Francisco: ASP), 11
McCook, G. P., & Sion, E. M. 1999, ApJS, 121, 1
Mohanty, S., & Basri, G. 2003, ApJ, 583, 451
Nakajima, T., Oppenheimer, B. R., Kulkarni, S. R., Golimowski, D. A., Matthews, K., & Durrance, S. T. 1995, Nature, 378, 463
Reid, I. N., Burgasser, A. J., Cruz, K. L., Kirkpatrick, J. D., & Gizis, J. E. 2001, AJ, 121, 1710
Reid, I. N., Kirkpatrick, J. D., Liebert, J., Gizis, J. E., Dahn, C. C., & Monet, D. G. 2002, AJ, 124, 519
Reipurth, B., & Clarke, C. 2001, AJ, 122, 432
Rosenthal, E. D., Gurwell, M. A., & Ho, P. T. P. 1996, Nature, 384, 243
Skrutskie, M. F., et al. 1997, in The Impact of Large-Scale Near-IR Sky Surveys, ed. F. Garzon et al. (Dordrecht: Kluwer), 25
Smith, V. V., et al. 2003, ApJ, 599, L107
Stephens, D. C., & Leggett, S. K. 2004, PASP, 116, 9

Testi, L., Natta, A., Sheperd, D. S., & Wilner, D. J. 2001, ApJ, 554, 1087
Tinney, C. G. 2000, in ASP Conf. Ser. 212, From Giant Planets to Cool Stars, ed. C. A. Griffith & M. S. Marley (San Francisco: ASP), 278
Tinney, C. G., Burgasser, A., Kirkpatrick, J. D., & Reid, I. N. 2003, AJ, 126, 975
Tinney, C. G., Delfosse, X., Forveille, T., & Allard, F. 1998, A&A, 338, 1066
Tinney, C. G., & Reid, I. N. 1998, MNRAS, 301, 1031
Tinney, C. G., & Tolley, A. J. 1999, MNRAS, 304, 119
Tokunaga, A. T., Simons, D. A., & Vacca, W. D. 2002, PASP, 114, 180